

AD-A239 549



2

TECHNICAL REPORT BRL-TR-3246

BRL

PENETRATION PERFORMANCE OF
TUNGSTEN ALLOY PENETRATORS WITH
L/D RATIOS OF 1 TO 1/32

TODD W. BJERKE
JONAS A. ZUKAS
KENT D. KIMSEY

DTIC
ELECTE
AUG 16 1991
S B D

JUNE 1991

APPROVED FOR PUBLIC RELEASE; DISTRIBUTION IS UNLIMITED.

U.S. ARMY LABORATORY COMMAND

BALLISTIC RESEARCH LABORATORY
ABERDEEN PROVING GROUND, MARYLAND

91-08012

01 0 15 025

NOTICES

Destroy this report when it is no longer needed. DO NOT return it to the originator.

Additional copies of this report may be obtained from the National Technical Information Service, U.S. Department of Commerce, 5285 Port Royal Road, Springfield, VA 22161.

The findings of this report are not to be construed as an official Department of the Army position, unless so designated by other authorized documents.

The use of trade names or manufacturers' names in this report does not constitute indorsement of any commercial product.

ERRATA FOR BRL-TR-3246

The discussion in section 4.1, pages 12 and 13, uses an incorrect expression for the pressure and particle velocity. The pressure relation should be

$$P = \rho_o U_s u_p$$

where ρ_o is the original material density, U_s is the shock wave velocity, and u_p is the particle velocity. The relationship between the shock velocity and the particle velocity is

$$U_s = 3.97 + 1.29 u_p$$

for the penetrator, and

$$U_s = 4.5 + 3.14 u_p$$

for the target (Kohn 1969). The interface pressure is obtained by the following procedure. An expression for the pressure balance at the interface of the penetrator and target is obtained by using the pressure relation and substituting for the shock velocity in each material. The particle velocity is solved for, which yields a shock velocity for the two materials. These are then used in the pressure relation to give the pressure the shock wave creates in the penetrator. The particle velocity is 1.16 km/s relative to a stationary observer. The shock velocity in the penetrator is 5.06 km/s, producing a pressure of 735 kb. The shock velocity is only slightly higher than the elastic wave velocity of 4.3 km/s in the penetrator, hence the transit times given on pages 12 and 13, and the number of wave transits listed in Table 6 are altered slightly. However, the conclusions drawn from the original values remain the same.

Reference:

Kohn, Brian J. "Compilation of Hugoniot Equations of State." AFWL-TR-69-38, Air Force Weapons Laboratory, Kirtland Air Force Base, NM, April 1969.

UNCLASSIFIED

REPORT DOCUMENTATION PAGE			Form Approved OMB No 0704-0188	
Public reporting burden for this collection of information is estimated to average 1 hour per response, including the time for reviewing instructions, searching existing data sources, gathering and maintaining the data needed, and completing and reviewing the collection of information. Send comments regarding this burden estimate or any other aspect of this collection of information, including suggestions for reducing this burden, to Washington Headquarters Services, Directorate for Information Operations and Reports, 1215 Jefferson Davis Highway, Suite 1204, Arlington, VA 22202-4302, and to the Office of Management and Budget, Paperwork Reduction Project (0704-0188), Washington, DC 20503.				
1 AGENCY USE ONLY (Leave blank)		2 REPORT DATE June 1991		3. REPORT TYPE AND DATES COVERED Final, Aug 90 - Feb 91
4 TITLE AND SUBTITLE Penetration Performance of Tungsten Alloy Penetrators With L/D Ratios of 1 to 1/32			5. FUNDING NUMBERS PR: 1L162618AH80	
6 AUTHOR(S) Todd W. Bjerke, Jonas A. Zukas, and Kent D. Kimsey			8 PERFORMING ORGANIZATION REPORT NUMBER	
7 PERFORMING ORGANIZATION NAME(S) AND ADDRESS(ES) U.S. Army Ballistic Research Laboratory SLCBBR-TB-P Aberdeen Proving Ground, MD 21005-5066				
9 SPONSORING / MONITORING AGENCY NAME(S) AND ADDRESS(ES) U.S. Army Ballistic Research Laboratory ATTN: SLCBBR-DE-T Aberdeen Proving Ground, MD 21005-5066			10. SPONSORING / MONITORING AGENCY REPORT NUMBER BRL-TR-3246	
11 SUPPLEMENTARY NOTES				
12a DISTRIBUTION / AVAILABILITY STATEMENT Approved for public release; distribution is unlimited			12b DISTRIBUTION CODE	
13 ABSTRACT (Maximum 200 words) A combined experimental and computational investigation was conducted to determine the terminal ballistic performance and transient behavior of low L/D tungsten alloy penetrators impacting normal incidence rolled homogeneous armor (RHA) targets at 2 km/s. Each penetrator had a nominal diameter of 25.4 mm, and an L/D of either 1, 1/2, 1/4, 1/8, 1/16, or 1/32. Experiments were performed using a 50-mm high pressure powder gun and a push-launch sabot. Data collected consisted of penetrator attitude and velocity at impact, depth of penetration, crater diameter, and limited information regarding residual penetrator material. Numerical simulations of each of the penetrators impacting RHA were performed with the Lagrangian code SMASH and the Eulerian code CTH. Both Codes exhibited good agreement with experimental data.				
14 SUBJECT TERMS terminal ballistics, kinetic energy projectiles, antiarmor ammunition, impact			15 NUMBER OF PAGES 85	
17 SECURITY CLASSIFICATION OF REPORT UNCLASSIFIED			16 PRICE CODE	
			20 LIMITATION OF ABSTRACT UL	
18 SECURITY CLASSIFICATION OF THIS PAGE UNCLASSIFIED		19 SECURITY CLASSIFICATION OF ABSTRACT UNCLASSIFIED		

INTENTIONALLY LEFT BLANK.

TABLE OF CONTENTS

	<u>Page</u>
LIST OF FIGURES	v
LIST OF TABLES	vii
ACKNOWLEDGMENTS	ix
1. INTRODUCTION	1
2. EXPERIMENTS	2
3. COMPUTATIONS	6
4. DISCUSSION	12
4.1 Wave Mechanics: Correlation With Experimental and Numerical Results ..	12
4.2 Numerical Considerations	22
5. CONCLUSIONS	24
6. REFERENCES	27
APPENDIX A: L/D 1 SMASH INPUT DECK	31
APPENDIX B: L/D 1/2 SMASH INPUT DECK	35
APPENDIX C: L/D 1/4 SMASH INPUT DECK	39
APPENDIX D: L/D 1/8 SMASH INPUT DECK	43
APPENDIX E: L/D 1/16 SMASH INPUT DECK	47
APPENDIX F: L/D 1/32 SMASH INPUT DECK	51
APPENDIX G: L/D 1 CTH INPUT DECK	55
APPENDIX H: L/D 1/2 CTH INPUT DECK	61
APPENDIX I: L/D 1/4 CTH INPUT DECK	67
APPENDIX J: L/D 1/8 CTH INPUT DECK	73
APPENDIX K: L/D 1/16 CTH INPUT DECK	79
APPENDIX L: L/D 1/32 CTH INPUT DECK	85

	<u>Page</u>
LIST OF SYMBOLS	91
DISTRIBUTION LIST	93

LIST OF FIGURES

<u>Figure</u>		<u>Page</u>
1.	One-Piece Frangible Sabot	5
2.	Sectioned Target Crater Profiles	7
3.	Residual Penetrators	9
4.	Predicted (CTH) Interface Pressure vs. Time for L/D = 1 Cylinder Impact	14
5.	Predicted (CTH) Pressure vs. Time at Rear of L/D = 1 Cylinder	14
6.	Predicted (SMASH) Pressure vs. Time History for Rear Surface of L/D = 1/2 and 1/4 Cylinders.	15
7.	Predicted (SMASH) Spallation of an L/D 1/2 Projectile	16
8.	Predicted (CTH) Pressure History for the Center of an L/D 1/32 Projectile	18
9.	Front and Rear Surface Displacement, L/D 1/16 Projectile	18
10.	Front and Rear Surface Displacement, L/D 1/32 Projectile	19
11.	Computed Penetration Crater, L/D 1 Penetrator	20
12.	Computed Penetration Crater, L/D 1/32 Penetrator	21
13.	Experimental and Computational P/L and P/E vs. L/D for 2 km/s Impact Velocity	23



Accession For	
NTIS GRA&I	<input checked="" type="checkbox"/>
DTIC TAB	<input type="checkbox"/>
Unannounced	<input type="checkbox"/>
Justification	
By	
Distribution/	
Availability Codes	
Dist	Avail and/or Special
A-1	

INTENTIONALLY LEFT BLANK.

LIST OF TABLES

<u>Table</u>	<u>Page</u>
1. Tungsten Alloy Static Properties	4
2. Penetrator Geometries	4
3. Performance of Low L/D Penetrators Impacting Semi-Infinite RHA	6
4. Residual Penetrator Measurements	9
5. Computational Results	11
6. Wave Transits in Cylindrical Projectiles.	17

INTENTIONALLY LEFT BLANK.

ACKNOWLEDGMENTS

The authors wish to acknowledge Ms. L. Luther, Mr. G. Lang, and Mr. W. Edmanson for their assistance and contributions with the experimental portion of this study.

INTENTIONALLY LEFT BLANK.

1. INTRODUCTION

The penetration performance of high density, low length-to-diameter ratio (L/D) penetrators impacting steel targets has been a topic of considerable interest to the armor/antiarmor community due to the speculated performance of a segmented rod penetrator munition. This has been spurred by the observation that relative penetrator performance (i.e., penetration per unit length [P/L]) increases as L/D decreases, provided that impact velocity is relatively high. Most of the research to date which substantiates this claim has focused on penetrators shaped as either spheres or right-circular cylinders with an L/D of one or slightly greater (Charters, Menna, and Piekutowski 1989; Charters 1987; Charters and Orphal 1989; Cline, Gogolewski, and Reaugh 1987; Cuadros 1989; Frank and Zook 1990; Hauver and Melani 1990; Hohler and Stilp 1990; Hohler and Stilp 1987; Holland et al. 1989; Hunkler 1990; Kivity, Yitzhak, and Hirsch 1989; Naz and Lehr 1989; Raatschen et al. 1987; Scheffler and Zukas 1989; Scheffler 1989; Sorensen et al. 1991; Tate 1990; and Zukas 1990a). The literature consists of a mix of experiments and computational simulations in which the trend of increasing P/L with decreasing L/D is conclusive for high density metallic penetrators impacting steel or aluminum targets. Denardo (1989) finds this trend to be true also for low L/D polyethylene cylinders impacting aluminum targets. Another trend evident from the literature is the dependence of segment performance upon impact velocity. Hauver and Melani (1990); Kivity, Yitzhak, and Hirsch (1989); Orphal, Anderson, and Franzen (1990); Raatschen et al. (1987); Scheffler and Zukas (1989); and Zukas (1990a) show through experiments and computations that low L/D segment performance increases dramatically with velocity and that a train of ideally spaced segments does not out-perform its monolithic rod counterpart until the impact velocity approaches or exceeds 2 km/s for tungsten-RHA impacts. Tate (1990) used the modified Bernoulli equation approach to develop an engineering model for a segmented penetrator in which the effects of segment spacings were also considered.

The performance of high density metallic penetrators with an L/D of less than one can be estimated by extrapolating the performance of higher L/D penetrators. Unfortunately, the inherent hazards of such extrapolations frequently lead to misleading or incorrect results. A limited number of investigations have considered penetrator shapes in which the L/D was less than one; however, these were performed at very small scale. Herbette (1989) noted a dramatic increase in P/L for steel disks with an L/D 1/30 impacting aluminum targets at 2 km/s

when compared to penetrators with considerably greater L/D. Orphal, Anderson, and Franzen (1989) and Orphal and Franzen (1990) also report a significant increase in P/L as penetrator L/D was reduced from 1 to 1/8 for tungsten, tungsten alloy, and tantalum alloy penetrators impacting steel at a velocity ranging from 1.5 to 7.5 km/s. Christman and Gehring (1966) fired aluminum and steel penetrators with an L/D ranging from 25 to 1/6 into metallic and non-metallic targets; however, their data was presented in such a manner that penetrator performance with relative L/D could not be interpreted. The Christman and Gehring data were also subject to large, uncontrolled penetrator pitch and yaw at impact. Denardo (1989) reported similar trends as the L/D of polyethylene penetrators were reduced from 1 to 1/6. Despite these studies, a full characterization and understanding of low L/D penetrator behavior has yet to be conducted.

In this study, a combined experimental and computational investigation was conducted to determine the terminal ballistic performance and transient behavior of low L/D tungsten alloy penetrators impacting normal incidence rolled homogeneous armor (RHA) targets at 2 km/s. Each penetrator had a nominal diameter of 25.4 mm, and an L/D of either 1, 1/2, 1/4, 1/8, 1/16, or 1/32. Experiments were performed using a 50-mm high-pressure powder gun and a push-launch sabot. Data collected consisted of penetrator attitude and velocity at impact, depth of penetration, crater diameter, and limited information regarding residual penetrator material. Numerical simulations of each of the penetrators impacting RHA were performed with the Lagrangian code SMASH (Kimsey and Zukas 1986) and the Eulerian code CTH (McGlaun and Thompson 1990). Both codes exhibited good agreement with experimental data.

2. EXPERIMENTS

A total of 13 shots were made in the BRL high pressure gun facility. Details of the facility are given by Bauer and Nagy (1979) and Silsby et al. (1983). The gun consists of a nominal 50-mm-diameter by 6-m-travel smooth bore powder gun with a large capacity, high pressure powder chamber. The gun empties into an impact chamber at atmospheric pressure. The target was located approximately 4.8 m from the gun muzzle.

One piezoelectric and two copper crush pressure transducers were located in the powder chamber of the gun to aid with the internal ballistic diagnostics of the gun. Two 150-kV orthogonal flash x-ray shadowgraph systems, located approximately 450 mm and 760 mm uprange of the target, were used to provide penetrator attitude and velocity data prior to impact. The x-ray systems required a means for detecting and enunciating the arrival of the penetrator at the x-ray stations (i.e., a properly timed trigger to activate each system). The trigger system employed was a "break-screen" placed approximately 300 mm uprange of the first x-ray station. The break-screen consisted of a piece of paper with a conductive etching on it, mounted to a thin piece of cardboard located on the shot-line of the gun. A voltage is applied across the etching and is monitored for interruptions. When the penetrator strikes the break-screen, it perforates the cardboard and interrupts the electrical circuit across the screen. This interruption activates the delay generators used to pulse the flash x-ray systems.

The penetrators were made from a 91% tungsten alloy (Teledyne Firth Sterling Alloy X-27) which was swaged to 25% reduction in area. The properties, static strengths, and composition of the alloy are listed in Table 1.

The penetrator geometries studied were right-circular cylinders with an L/D ratio of either 1/2, 1/4, 1/8, 1/16, or 1/32. The diameter of each penetrator was nominally 25.4 mm, except for the L/D 1/2 penetrator which was 29.1 mm. An L/D=1 penetrator with a diameter close to 25 mm was not fired because it was too massive for the sabot system used for this program; hence, its performance was determined from calculations. The nominal mass and dimensions for each of the different L/D penetrators are listed in Table 2.

Right-circular, low L/D penetrators are highly unstable during flight and prone to tumbling. Conventional push- or traction-launch sabots release the penetrator soon after muzzle exit, which provides ample time for penetrator tumbling to occur, resulting in high yaw at impact. In order to achieve low yaw at impact, a different sabot technique was employed. A one-piece frangible sabot made from 6/6 Nylon, Figure 1, was used. The sabot had an overall L/D of approximately one and served as the flight body for the penetrator after muzzle exit. The penetrator was placed in a cavity machined into the front of the sabot. The relatively high-mass penetrator acted as a nose weight which yielded an aerodynamically stable sabot-penetrator assembly. The penetrator was released from the sabot on impact with the break-

Table 1. Tungsten Alloy Static Properties

Density:	17,270 kg/m³
Hardness:	39.1 HRC
Tensile Properties	
0.2% Offset Yield Strength:	1.09 GPa
Ultimate Strength:	1.11 GPa
Total Elongation to Failure:	9.7%
Compression Properties	
0.2% Offset Yield Strength:	0.95 GPa
1.0% Offset Yield Strength:	1.16 GPa
Composition (by Weight)	
Tungsten:	91.0%
Nickel:	6.3%
Iron:	2.7%

Table 2. Penetrator Geometries

L/D	Mass (g)	Thickness (mm)	Diameter (mm)
1/2	150.4	12.95	29.13
1/4	55.6	6.35	25.40
1/8	27.6	3.17	25.40
1/16	13.8	1.60	25.40
1/32	6.8	0.79	25.40

screen. The impact forces shattered the Nylon sabot, causing the debris to spread radially, falling behind and leaving the penetrator undisturbed. The short flight distance which remained was not sufficient for penetrator tumbling to occur. This technique provided a reliable means for delivering disk-shaped penetrators to a target with proper impact orientation and negligible contribution by the sabot to penetration.

The targets were monolithic blocks of RHA with a nominal height and width of 200 mm and a thickness of 150 mm. The measured hardness of the targets ranged from 241 to 277 BHN. The targets were placed in the impact chamber such that the obliquity (the angle

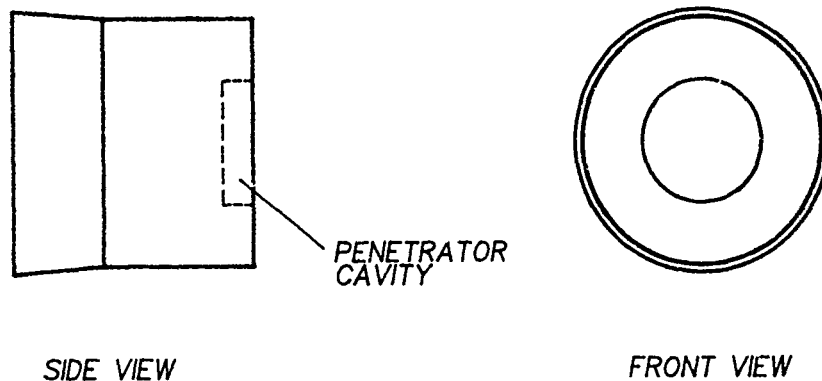


Figure 1. One-Piece Frangible Sabot.

between the target face normal and the shot line) was less than one degree and the penetrator would impact the center of the target face.

The ballistic test procedure used was typical of conventional ballistic range impact testing in that the penetrator was accelerated to the desired velocity in the gun, permitted to pass through the instrumentation field, and its flight then terminated by impact with the target. Projectile velocity, yaw, and yaw rate measurements were obtained from the x-ray shadowgraphs and associated timing information. The projectile velocity was assumed not to decrease significantly during the short flight distance between the x-ray stations and the target; hence, the velocity obtained from the x-ray systems was used as the impact velocity. Penetrator yaw at impact was determined by assuming a constant yaw rate between the x-ray locations and the target. A summary of the experimental results, including velocity and yaw, is presented in Table 3.

Post-test impact crater measurements consisted of crater depth (P) and crater diameter (H). Impact crater depths were measured with a depth micrometer probe. The measured

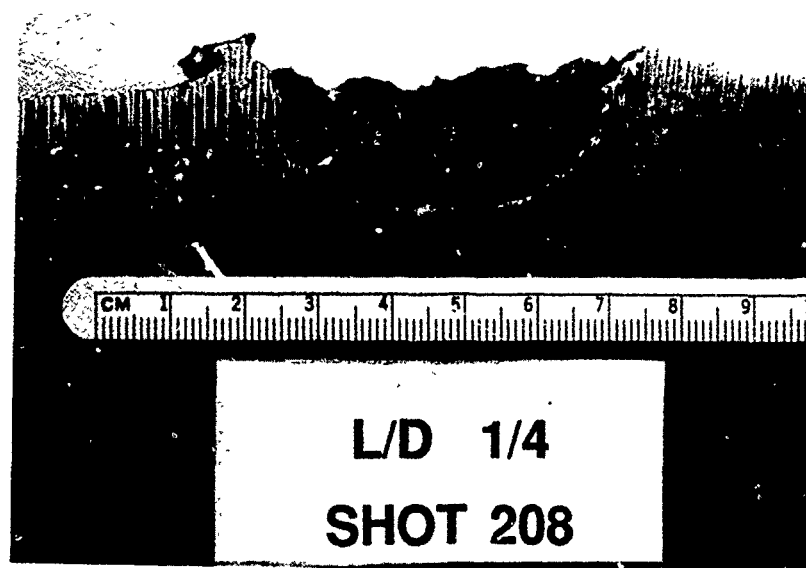
Table 3. Performance of Low L/D Penetrators Impacting Semi-Infinite RHA

Shot No.	L/D	Velocity (m/s)	Yaw (deg)	P (mm)	P/E (mm/MJ)	P/L	H (mm)
194	1/2	2,042	4.3	33.0	105.2	2.5	66.0
206	1/4	2,100	4.0	19.3	157.4	3.0	49.8
207	1/4	2,044	1.2	19.6	168.7	3.1	51.8
208	1/4	2,015	3.8	18.1	160.3	2.8	55.9
216	1/8	1,931	3.0	13.1	254.6	4.1	37.3
204	1/8	2,040	7.4	16.4	285.6	5.2	39.4
221	1/8	2,036	2.3	18.5	323.4	5.8	41.9
222	1/8	1,996	2.0	13.1	238.3	4.1	41.4
217	1/16	2,004	10.4	6.9	249.0	4.3	29.5
219	1/32	1,958	12.6	2.3	176.5	2.9	27.9

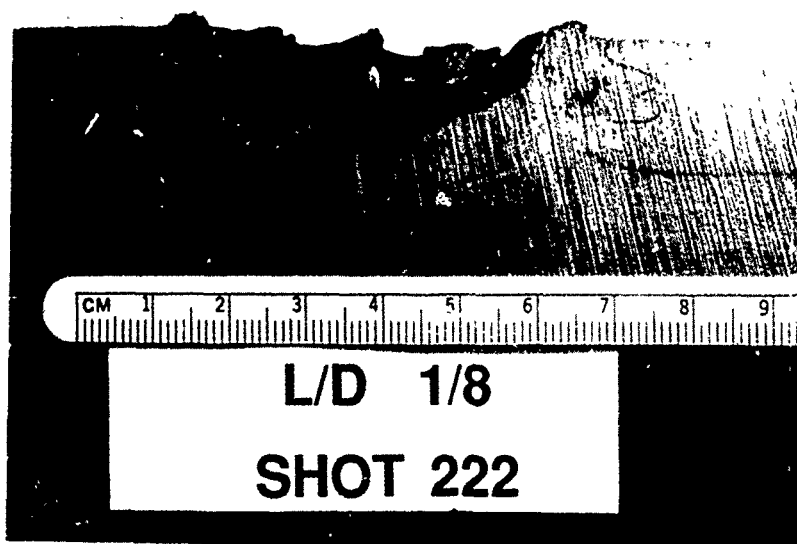
depths were made relative to the undisturbed surface of the impacted target face. The diameter of each crater was also measured; however, this measurement was subjective due to the sloping walls of the relatively shallow craters. The diameter was typically measured slightly below the target surface. The post-test crater measurements are included in Table 3. Penetration depths normalized by penetrator length and by penetrator kinetic energy at impact are also included in Table 3. A representative target for each of the different L/D penetrators (except L/D 1/2) was sectioned and photographed and are shown in Figure 2. Residual penetrator material was recovered for one shot with an L/D 1/4 penetrator and two shots with an L/D 1/8 penetrator. These were weighed, measured, and photographed. The recorded data are listed in Table 4, and a photograph of a representative recovered penetrator for L/D 1/4 and 1/8 is shown in Figure 3. The diameter listed in Table 4 is an estimated diameter based upon the general shape of the recovered penetrator.

3. COMPUTATIONS

Lagrangian calculations of low L/D projectiles impacting semi-infinite RHA were performed with SMASH, a local variant of the EPIC-2 code (Johnson 1978) modified to include eroding slide-line logic (Kimsey and Zukas 1986). Dynamic material properties for the tungsten alloy

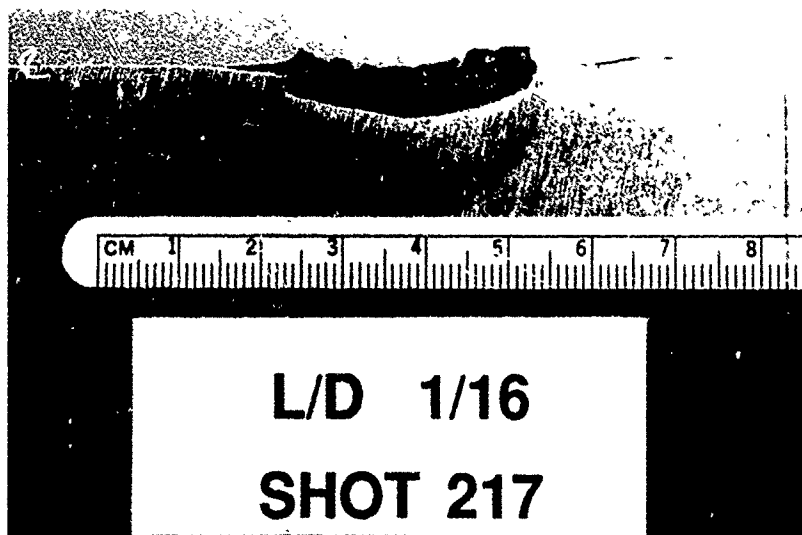


(a) Shot 208; L/D 1/4

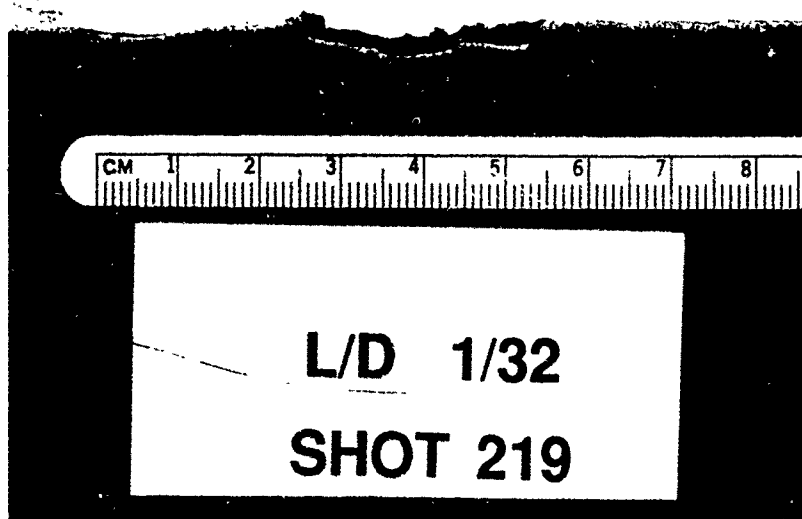


(b) Shot 222; L/D 1/8

Figure 2. Sectioned Target Crater Profiles.



(c) Shot 217; L/D 1/16

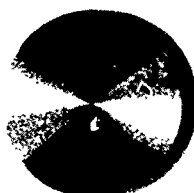
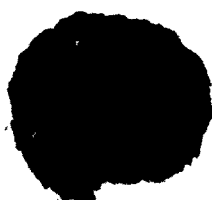


(d) Shot 219; L/D 1/32

Figure 2. Sectioned Target Crater Profiles (Continued).

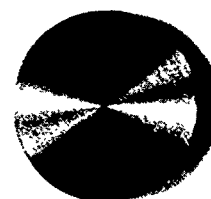
Table 4. Residual Penetrator Measurements

Shot No.	L/D	Thickness (mm)	Estimated Diameter (mm)	Mass (g)	Fraction of Mass Recovered (%)
206	1/4	3	30	19.7	35.4
202	1/8	3	25	12.8	46.4
204	1/8	3	25	17.9	64.9



L/D 1/8

(a) Shot 204



L/D 1/4

(b) Shot 206

Figure 3. Residual Penetrators.

projectiles were taken from split-Hopkinson bar data reported by Nicholas (1980) for 90W-7Ni-3Fe, 25% swaged. The yield stress for the tungsten was taken to be 14 kbar and the ultimate stress to be 19.3 kbar. The RHA target material was modeled as an elastic perfectly plastic material with a flow stress of 7.0 kbar (Benck and Robitaille 1977). A power series form of the Mie-Grüneisen equation-of-state was used to define pressure-volume states, and the appropriate parameters for tungsten alloy and steel were taken from Kohn (1969).

Two levels of failure may be modeled with the version of EPIC used for these studies, based on user-specified levels of effective plastic strain. When the first level is met, tensile and shear stresses are not allowed to develop in the affected elements. The net result is that the element behaves much like a liquid in that it can support only hydrodynamic compression. When the second level of effective plastic strain is reached, all stresses and pressures are set to zero. Element quantities are no longer included in the simulation, as though total failure had occurred. When this option is invoked, mass and momentum continue to be conserved since the masses and velocities of the failed elements are associated with their nodes, and these are tracked throughout the computation. Energy, however, is conserved only approximately since element internal energies are no longer computed. This is a minor concern, however, since this latter value of strain is set at high (150–250%) levels (for lack of better failure models) so that elements "removed" from the calculation would, in reality, appear as ejecta in ballistic experiments.

The grid for the calculations was made up of four constant strain triangles per quadrilateral. The total number of nodes for the calculation approached 15,000 while the total number of elements was close to 30,000. As a rule, between 10 and 25 layers of quadrilateral elements were used through the thickness of the projectile, the number of elements in the radial direction being adjusted to maintain a 1:1 aspect ratio. The target block had a radius of 60 mm and a depth of 100 mm, effectively simulating a semi-infinite block. Some calculations were redone with a target radius of 100 mm, but these showed no appreciable difference from the calculations with a radius of 60 mm. SMASH input data for the cases modeled are presented in Appendices A–F, and the computational results are shown in Table 5.

A duplicate set of calculations were performed with the Eulerian code CTH (McGlaun and Thompson 1990) for comparison. CTH is a family of computer programs for modeling solid dynamics problems involving shock wave propagation, multiple materials, and large deformations in one, two, and three dimensions. The code solves the finite-difference analogs of the conservation equations for mass, momentum, and energy. A high resolution interface tracker is used to minimize material dispersion, and a second-order convection scheme is used to flux all quantities between cells. The material model is elastic perfectly plastic with linear thermal softening. Material failure is based on maximum pressure or principal stress.

Table 5. Computational Results

L/D	L (mm)	P SMASH (mm)	P/L SMASH	P CTH (mm)	P/L CTH
1	25.40	50.8	2.0	54.0	2.1
1/2	12.70	27.9	2.2	32.0	2.5
1/4	6.35	21.6	3.4	20.0	3.2
1/8	3.18	16.2	5.1	13.0	4.1
1/16	1.59	7.5	4.8	6.5	4.1
1/32	0.79	3.0	3.8	2.4	3.0

Both analytical and tabular equations-of-state are available for modeling the hydrodynamic behavior of solid materials. In addition, a programmed burn model is available for modeling high explosive detonation.

The CTH simulations reported herein used a linear Hugoniot shock-particle velocity equation-of-state to model the hydrodynamic behavior of the materials. An elastic perfectly plastic model is the only plasticity model currently implemented in CTH. Therefore, the dynamic yield strengths for both the penetrator (19.3 kbar) and target (7.0 kbar) materials used for the Lagrangian calculations were used for the Eulerian calculations.

The CTH simulations used a cylindrical coordinate system with a semi-infinite RHA target. The multiple material temperatures and pressures thermodynamic model was used to calculate separate temperatures and pressures for each material in multimaterial cells. A high resolution interface algorithm was used to define material interfaces and minimize material dispersion in multimaterial cells.

The zoning for the CTH simulations employed square cells in the penetrator-target interaction region. Typically, 5–10 cells were used through the thickness of the penetrator (e.g., 1.06-mm by 1.06-mm cells were used for the L/D=1 penetrator model and 0.08-mm by 0.08-mm cells were used for the L/D=1/32 penetrator model). The total number of cells in a model ranged from 30,000 to 148,125. Typically, the radial and axial boundaries of the target were placed approximately 5 penetrator diameters from the impact point. Transmitting

boundary conditions were used at the radial and axial edges of the mesh. The CTH input data for all L/D cases modeled are provided in Appendices G–L, and the computational results are summarized in Table 5.

4. DISCUSSION

4.1 Wave Mechanics: Correlation With Experimental and Numerical Results. The experimental and computational results indicate that the behavior of low L/D segments can be loosely grouped into three categories:

- (1) rod-like response ($L/D > 1$)
- (2) transitional - aspects of both rod and plate behavior ($1 > L/D > 1/8$)
- (3) plate-like response ($L/D < 1/8$)

These can best be illustrated using elementary concepts from wave mechanics. For a background in this area, see Johnson (1972), Wasley (1973), Rinehart (1975), Zukas et al. (1982), and Zukas (1990b).

Consider a cylindrical projectile with $L/D=1$. Upon impact, a compression wave is propagated into both target and projectile with an initial intensity of $\rho c v$ where ρ represents density, c the sound speed in the material, and v the particle velocity. For like-material impacts, $v = V_s/2$, where V_s is the striking velocity. For dissimilar material impacts, v can be determined from

$$v = V_s / [1 + (\rho_t c_t) / (\rho_p c_p)] ,$$

where subscripts t and p refer to target and projectile, respectively. For a tungsten alloy projectile ($\rho = 17.3 \text{ g/cm}^3$; $c = 0.4 \text{ cm}/\mu\text{s}$) striking an RHA plate ($\rho = 7.8 \text{ g/cm}^3$; $c = 0.55 \text{ cm}/\mu\text{s}$) at a velocity of 2 km/s , $v = 0.12 \text{ cm}/\mu\text{s}$, and the pressure in the penetrator $= \rho c v = 830 \text{ kbar}$. Almost immediately upon impact, relief waves propagate in from the lateral free surfaces. After a time $t = r/c \approx 3.2 \mu\text{s}$, relief waves from the radial boundary will have reached the center of the projectile and diminished the magnitude of the initial compressive pulse. The original compressive pulse will reach the rear surface of the projectile at a time $t = L/c \approx 6.4 \mu\text{s}$. By this time, a fully two-dimensional stress state will have been

developed in the projectile with a pressure amplitude considerably less than the peak pressure first experienced on impact. This is shown in Figures 4 and 5, which are plots of pressure as a function of time at two locations in the projectile—the projectile-target interface and the rear surface of the rod.

Shortly after $t = L/c$, the pulse is reflected from the rear of the projectile and returns to the projectile-target interface at $t = 2L/c$. Thence, due to the impedance mismatch between the projectile and target, a portion of the pulse is transmitted into the target, the remainder being reflected back into the projectile. Wave reverberations in the radial direction in the projectile continue as well so that, until consumed or arrested, the $L/D=1$ projectile will experience a two-dimensional stress state which, after the first wave reverberations, is too complex to describe analytically but can readily be tracked numerically (e.g., Zukas and Segletes 1989).

Note that the computer calculations account for two-dimensional geometric effects, pressure pulses with finite rise times, and changes in sound speed with compression. Thus, there will be small differences in arrival times between those from elementary wave theory and numerical computations. The basic phenomena, however, remain the same.

As the projectile length and L/D ratio decreases (D being fixed in this case), there begins a transition from rod-like behavior (two-dimensional stress state) which is characteristic of long rod penetrators to plate-like behavior (uniaxial strain) for a significant portion of the plate-projectile response. This can be appreciated from Table 6, which compares the number of wave transits in the radial direction ($r = 1.27$ mm for all cases) to the number of wave transits in the axial direction with decreasing L/D . Thus, for $L/D=1$, in the time the radial release wave has traversed a distance r , the axial wave has only completed 1/4 of its passage through its path $2L$. By contrast, for $L/D= 1/32$, there will be eight complete transits in the axial direction before the arrival at the projectile center of the radial release wave.

Figure 6 shows the pressure-time history at the rear of the $L/D=1/2$ and $1/4$ projectiles. A large compressive pulse arrives at the rear surface and is immediately reflected in tension. This tensile state is maintained for a considerable period, being reinforced by tension from the radial release wave, resulting in spallation of the projectiles (illustrated in Figure 7). Residual

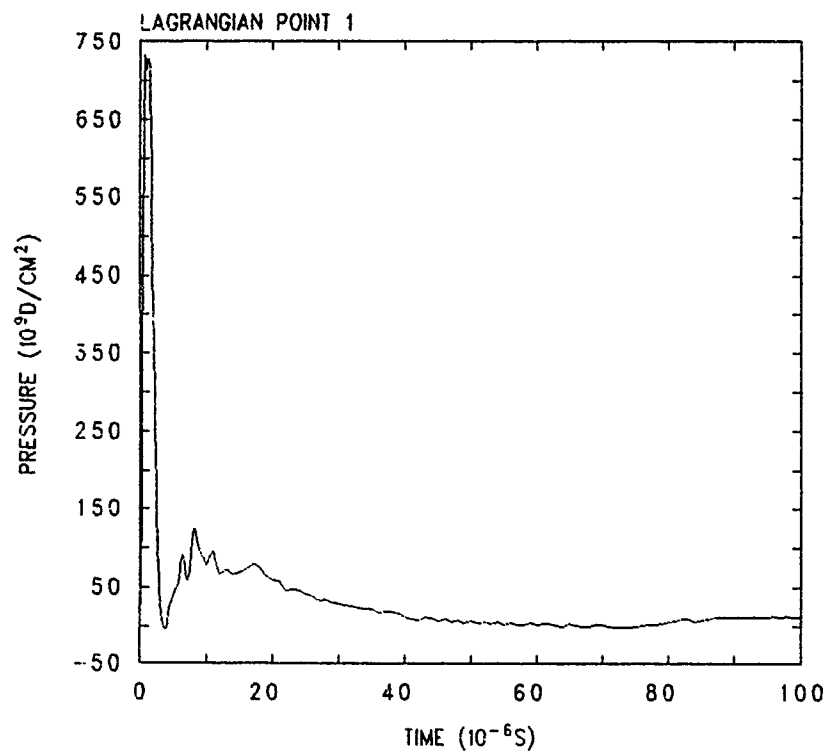


Figure 4. Predicted (CTH) Interface Pressure vs. Time for L/D=1 Cylinder Impact.

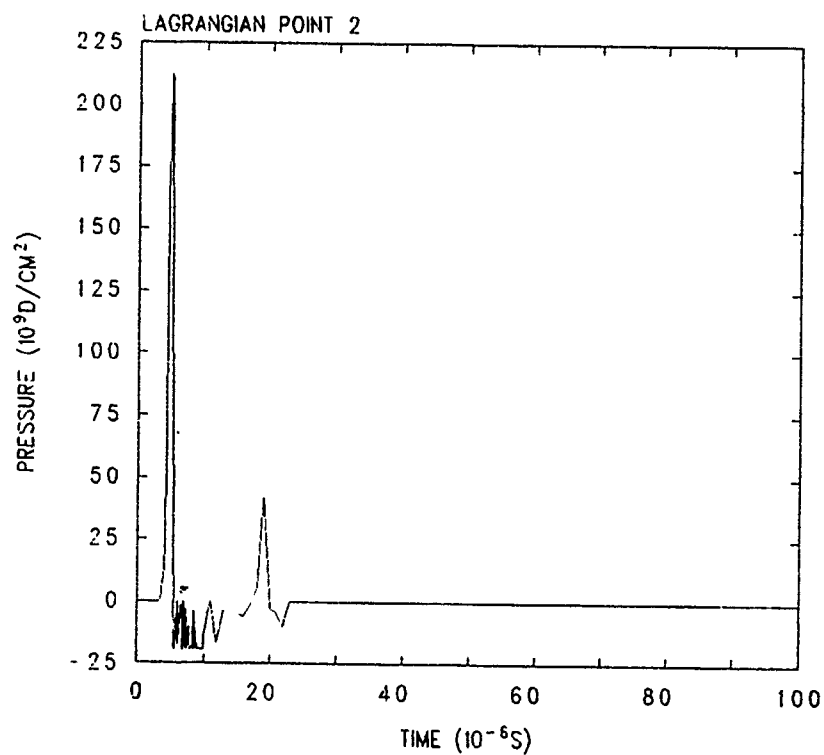
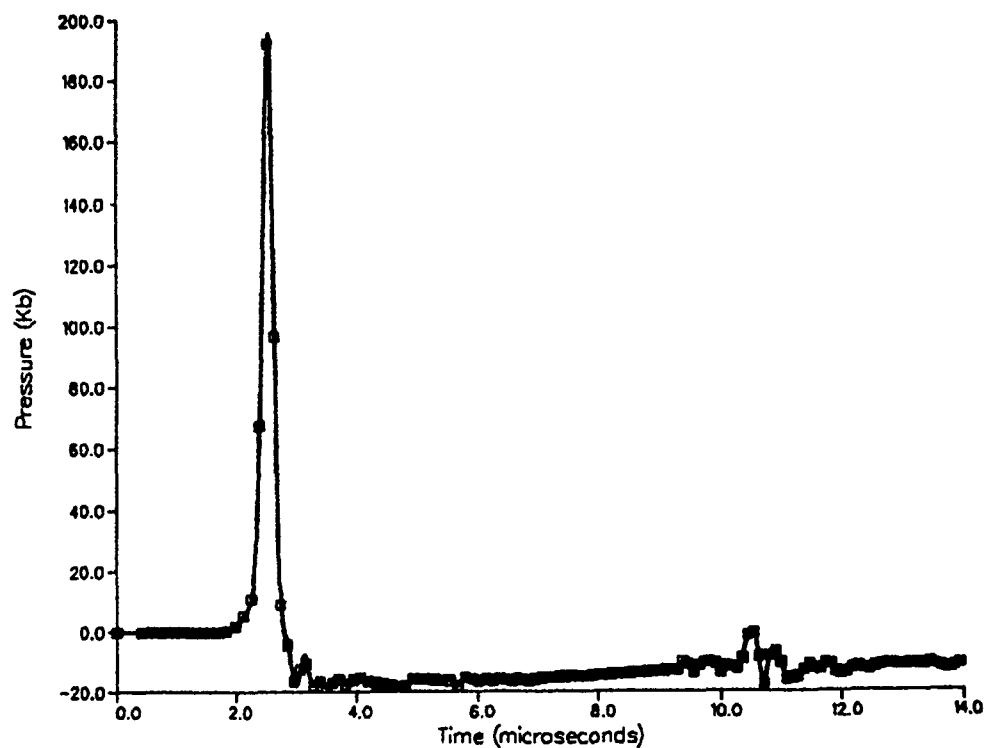
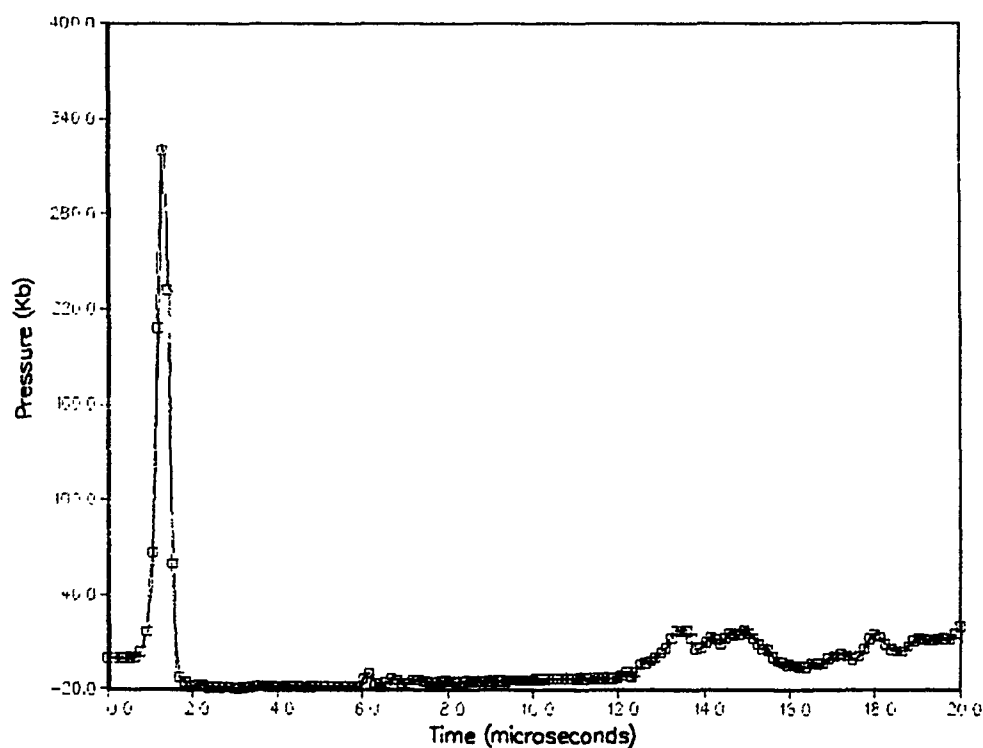


Figure 5. Predicted (CTH) Pressure vs. Time at Rear of L/D=1 Cylinder.

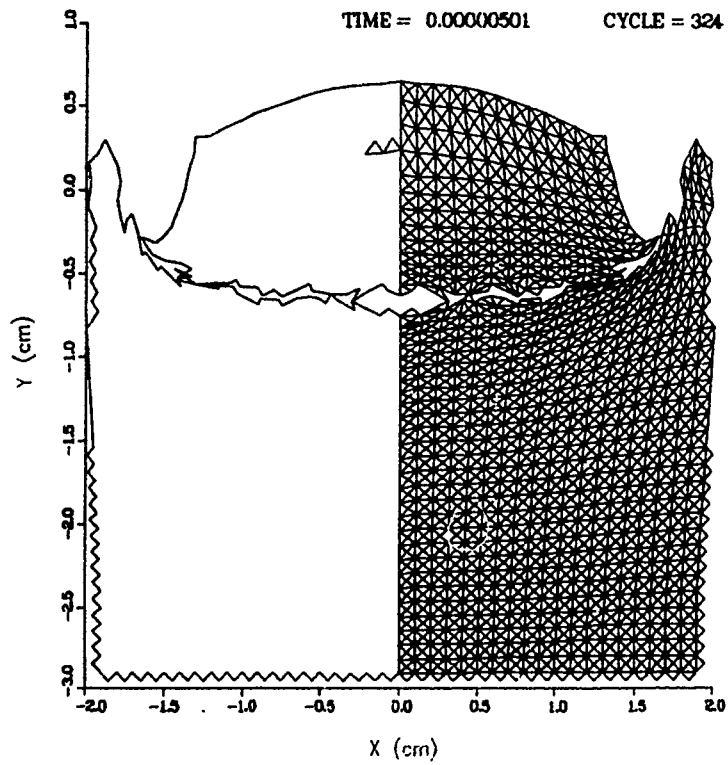


(a) $L/D = 1/2$

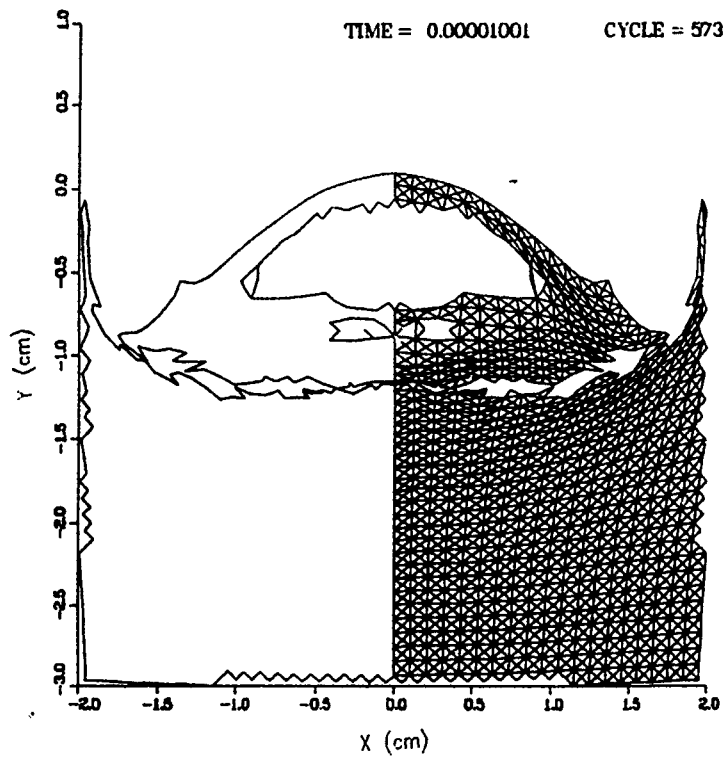


(b) $L/D = 1/4$

Figure 6. Predicted (SMASH) Pressure vs. Time History for Rear Surface of $L/D=1/2$ and $1/4$ Cylinders.



(a) L/D 1/2 Projectile at 5 μ s



(b) L/D 1/2 projectile at 10 μ s

Figure 7. Predicted (SMASH) Spallation of an L/D 1/2 Projectile.

Table 6. Wave Transits in Cylindrical Projectiles

L/D	No. of Radial Transits	No. of Axial Transits
1/1	1	1/4
1/2	1	1/2
1/4	1	1
1/8	1	2
1/16	1	4
1/32	1	8

Note: Distance traveled in the radial direction = $r = 1.27$ mm.
Distance traveled in the axial direction = $2L$.

projectiles were recovered for the $L/D=1/4$ and $1/8$ experiments and measured 0.3 cm thick, compared to numerically computed thicknesses of 0.25 cm.

For $L/D \leq 1/8$, a state of uniaxial strain is approached in the central region of the projectile. The decreased projectile length permits numerous wave reverberations in the axial direction before the arrival of the radial wave so that an effective uniaxial strain state is maintained for quite some time. Rapid unloading of the initial peak pressure occurs (see Figure 8), and the short duration of high amplitude pressure waves inhibit spall. There is slight radial expansion of the projectile but little to no contraction in the axial direction. This is evident from a time history plot of the front and rear surfaces of L/D 1/16 and 1/32 penetrators (shown in Figures 9 and 10). The vertical distance between the front and rear surface curves on each plot indicate penetrator thickness. The penetration crater, which for the $L/D=1$ case resembles that of a stubby cylindrical projectile (Figure 11), is flat for the L/D 1/32 case (Figure 12). Considerable penetrator flexure was also observed for the $L/D \leq 1/8$ numerical simulations. An example of the mode of flexure is shown in Figure 12a. A section of the penetrator near the radial center temporarily loses contact with the target surface. This was observed in both codes but was more pronounced in the Lagrangian simulations.

The experimental and computational results show that the maximum penetration per unit length, or length efficiency of the penetrator (P/L), is achieved for penetrators with an L/D of about 1/8. A plot of P/L values obtained from experiment and computations as a function of

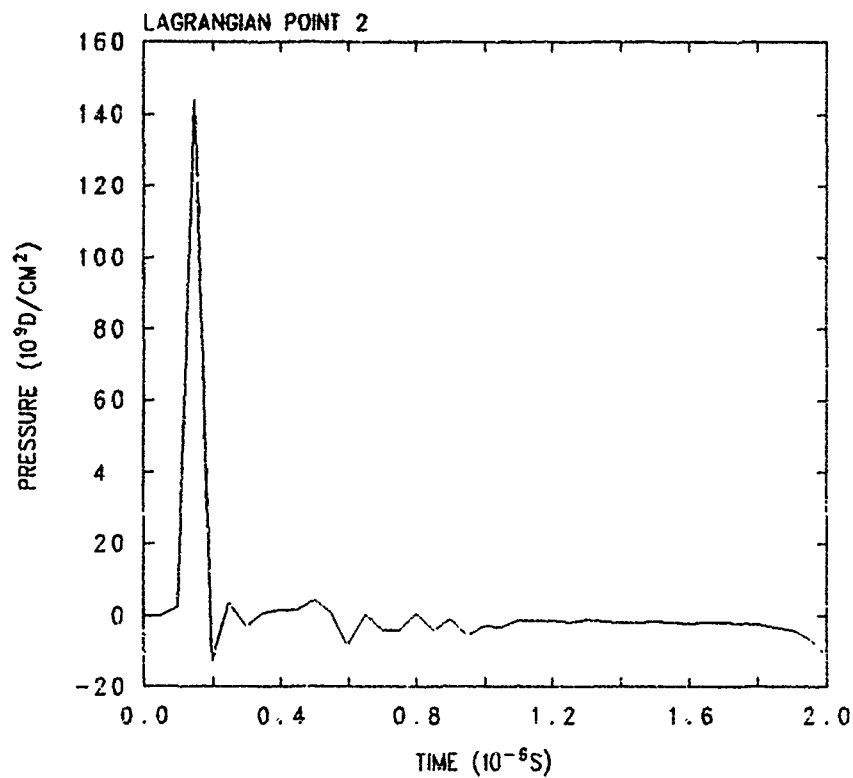


Figure 8. Predicted (CTH) Pressure History for the Center of an L/D 1/32 Projectile.

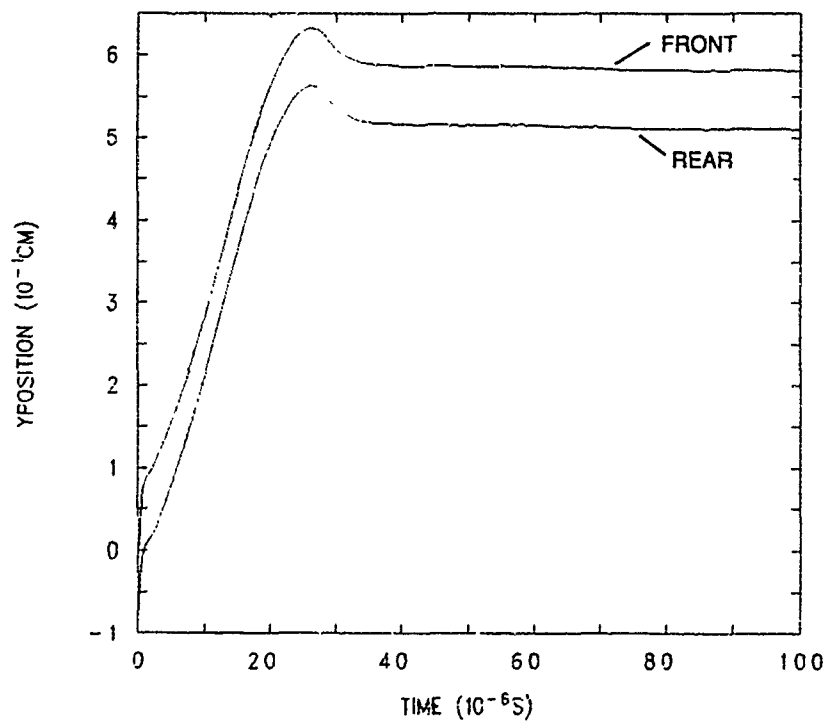


Figure 9. Front and Rear Surface Displacement, L/D 1/16 Projectile.

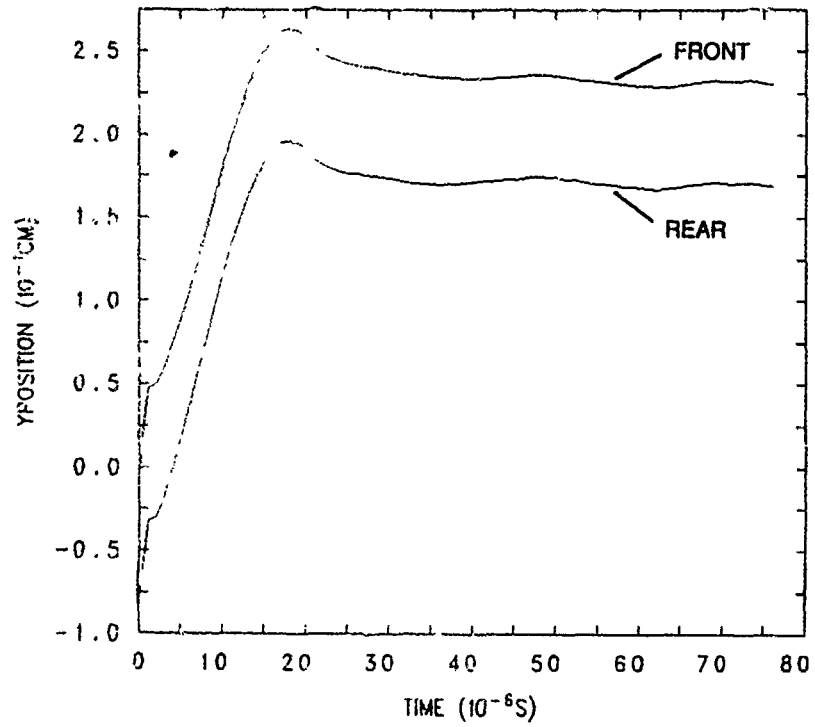
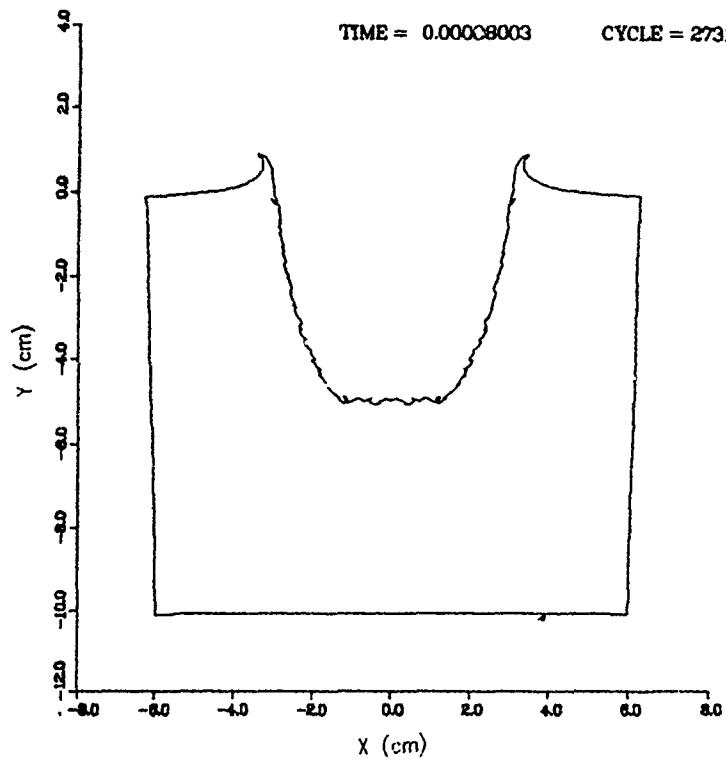
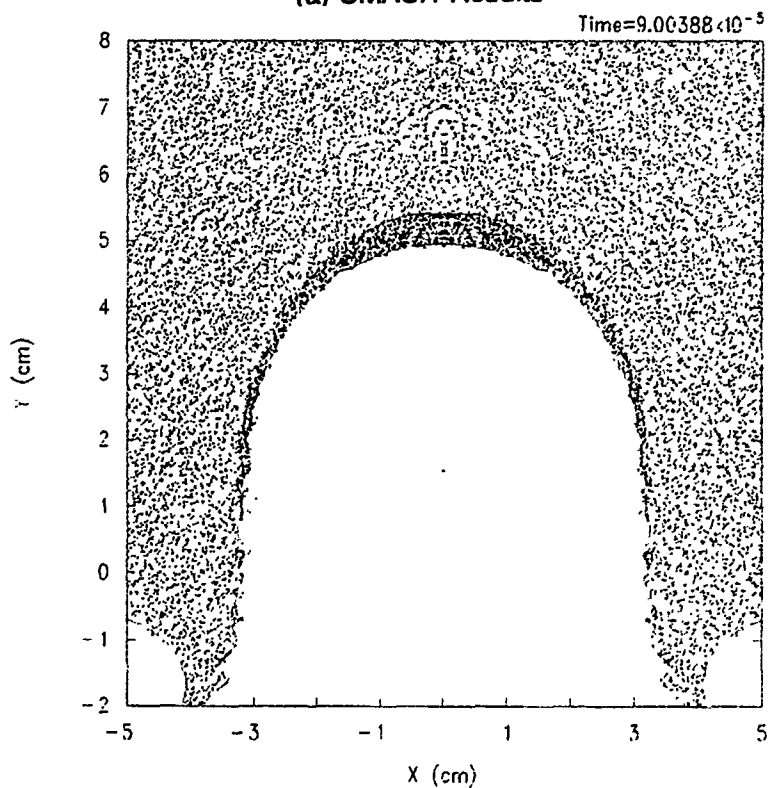


Figure 10. Front and Rear Surface Displacement, L/D 1/32 Projectile.

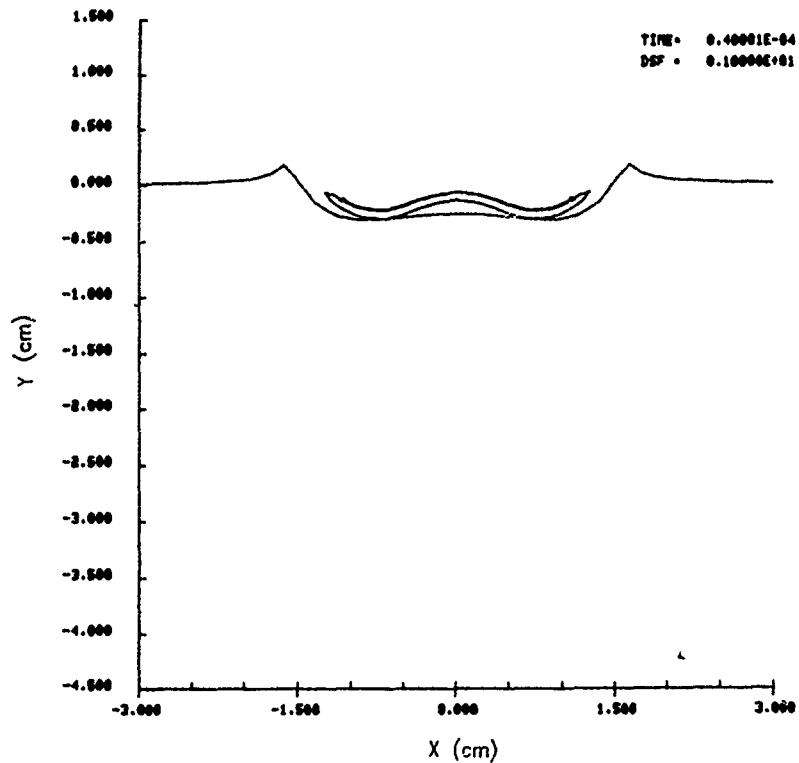


(a) SMASH Results

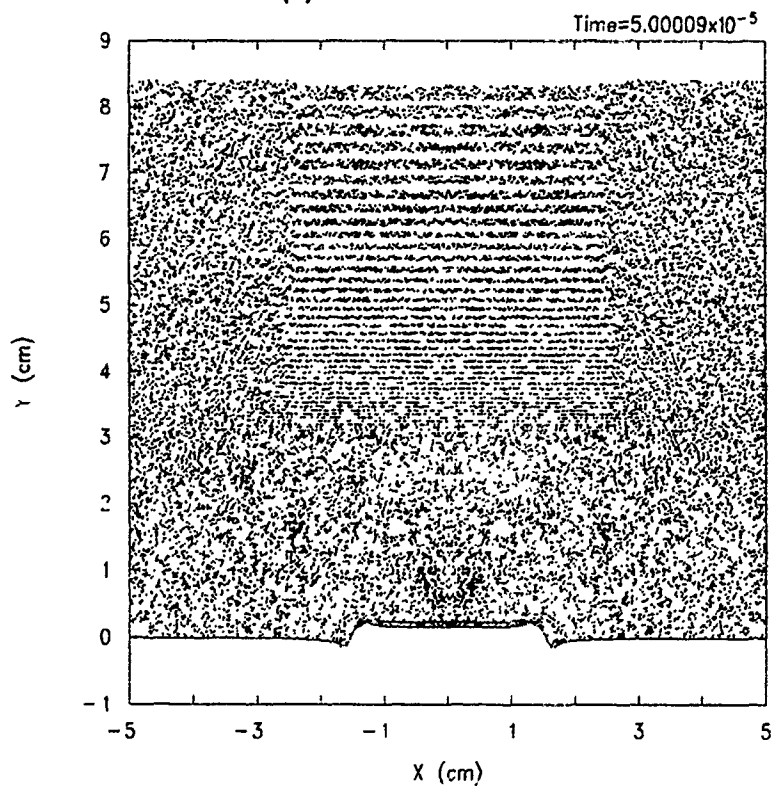


(b) CTH Results

Figure 11. Computed Penetration Crater, L/D 1 Penetrator.



(a) SMASH Results



(b) CTH Results

Figure 12. Computed Penetration Crater, L/D 1/32 Penetrator.

L/D is shown in Figure 13. A moderate degree of scatter exists in the experimental data, especially for the L/D 1/8 shots. There is only a slight discrepancy in the results obtained from the two computer codes. However, experiments and computations show the same trends and agree quite well.

Another way of measuring penetrator "efficiency" is to consider penetration normalized by penetrator kinetic energy, P/E, at impact. P/E is related to P/L by the following relation:

$$P/E = P/L [8 / (\pi \rho_p D^2 V_s^2)]$$

Penetrator diameter and impact velocity were held constant in this study; hence, penetrator energy efficiency is linearly related to length efficiency. Therefore, Figure 13 also indicates the trend of P/E with velocity. As can be seen in Figure 13 (and Table 3), a penetrator with an L/D of 1/32 is more energy efficient than a penetrator with an L/D of 1/2 or 1, and the penetrator with the greatest energy efficiency is one with an L/D of approximately 1/8.

An important point to note is that the ratio P/L does NOT tend to infinity as L approaches zero. The transition from rod mechanics to plate mechanics should preclude this, at least at velocities at or below 2 km/s. The plot of P/L vs L/D (Figure 13) shows a peak of non-dimensional penetration at L/D=1/8, then a decline. This suggests that while penetration tends to zero as L tends to zero, there is a point, dependent upon projectile material, geometry, and striking velocity, where P approaches zero at a greater rate than L approaches zero. A similar argument can be made on the basis of projectile kinetic energy. As projectile mass tends to zero, projectile energy tends to zero. Thus, projectile penetration must inevitably tend to zero. The case of zero projectile mass will never be achieved in practice. Nevertheless, with reduced projectile mass (decreasing L), the accompanying penetration will decline from a measurable quantity to mere scratches on the target surface.

4.2 Numerical Considerations. As Figures 4, 5, and 8 indicate, the transient loading which results from the high-velocity impact of a low L/D tungsten alloy projectile with an RHA target is analogous to shock loading. There is a sharp compressive pressure spike followed by rapid tensile unloading (both events occurring in a time frame of $2L/c$) and then oscillations about a mean value near the material strength which last for the bulk of the response time.

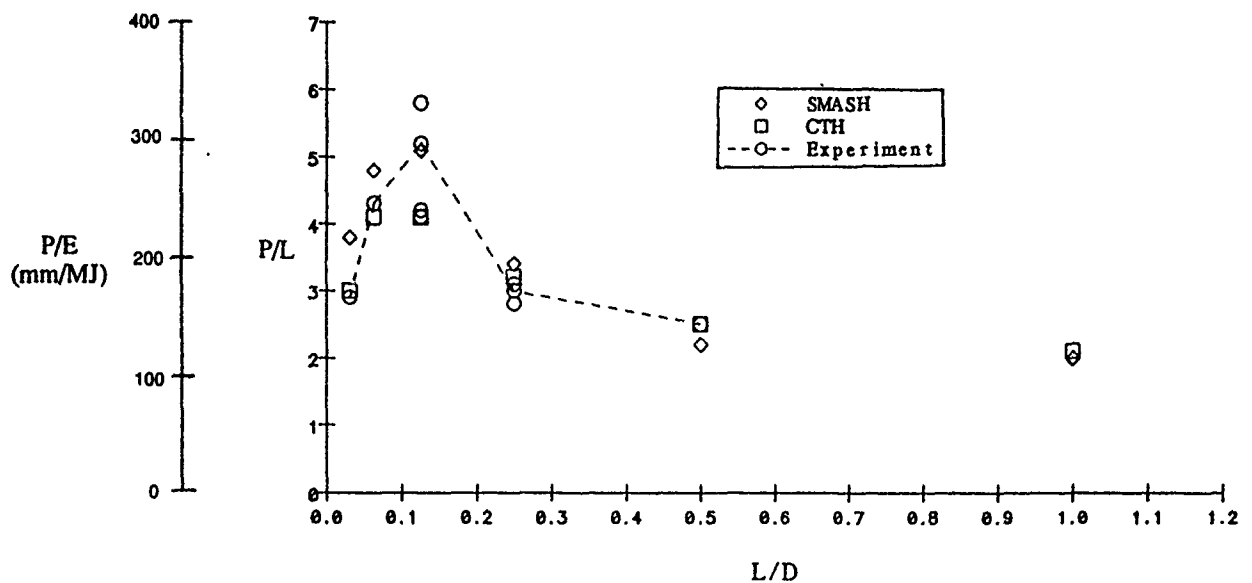


Figure 13. Experimental and Computational P/L and P/E vs. L/D for 2 km/s Impact Velocity.

Adequate resolution of this pressure spike requires a very fine spatial grid in the projectile. Most calculations with SMASH were run with at least 10 elements through the projectile length, the number of elements in the radial direction being adjusted to maintain a 1:1 aspect ratio. With this spatial resolution, SMASH predicted a peak impact pressure of 850 kbar, compared to 830 kbar predicted from elementary wave theory. CTH computed a peak value of 735 kbar. Considering the differences between the Lagrange and Euler computational techniques as well as the different forms of the Mie-Grüneisen equation-of-state, the results from both codes are equivalent.

Failure to maintain adequate spatial resolution has other deleterious effects. In Euler calculations, diffusion increases with increasing cell size, leading to the presence of more and more mixed cells. While the multiple material temperature and pressure thermodynamic model was used in the Euler calculations, pressure-time histories at user-specified data-collection points were obtained from interpolations between cell-centered values which only approximate the pressure at material interfaces. Lagrange calculations employing eroding slideline logic, such as SMASH, can suffer from excessive material loss and pressure

oscillations at the interface. For calculations which use a relatively coarse grid, the pressure-time history is computed incorrectly, and the mass removed by the erosion algorithm is overestimated. The zoning used in projectile and target in these numerical simulations is believed to be the minimum required to accurately predict the residual length or spall thickness as well as peak impact pressure.

The key to successful computations of the impact response of low L/D projectiles at high velocity is

- high spatial resolution
- material data for the constitutive law from dynamic (wave propagation) experiments.

The former implies a minimum of 10 elements through the projectile length and maintaining a 1:1 aspect ratio of the elements in zones undergoing large deformations or experiencing steep pressure gradients. To minimize spurious pressure oscillations resulting from the contact-impact (slideline) algorithm, approximately equal nodal masses should be maintained on each side of a slideline. This requirement imposes a restriction on the maximum element size in the target (assuming the projectile grid to be fixed) in the vicinity of steep gradients of pressure or deformation and, thus, sets the requirement for the total number of elements in a calculation. For good agreement with experiment, nearly 30,000 elements were required for the Lagrangian calculations in both projectile and target. For most calculations fewer than 2,000 elements were required to describe projectile geometry. The Eulerian calculations used between 30,000 and 148,125. The requirement for dynamic material property data for the penetrator and target materials was satisfied by using split-Hopkinson bar data, determined at strain rates between 100 and $1,000 \text{ s}^{-1}$ (Nicholas 1980) for the deviatoric behavior, and a high-pressure equation-of-state based on Hugoniot data for the volumetric response (Kohn 1969).

5. CONCLUSIONS

For the cases studied here (impact velocity of 2 km/s; tungsten alloy projectiles vs. semi-infinite RHA; projectile length-to-diameter ratios ranging from 1 to 1/32), the following conclusions apply:

- (1) The mechanics of deformation for the projectile change from rod-like behavior to plate-like behavior as L/D decreases.
- (2) Projectiles with an $L/D = 1/2$ and $1/4$ are observed to spall. For $L/D \leq 1/8$, the pressure is attenuated too rapidly for spall to occur. For projectiles with $L/D \geq 1$, relief waves from the lateral free surfaces provide stress relief which eliminate projectile spalling.
- (3) Projectiles with $L/D \leq 1/8$ show slight lateral expansion and negligible length reduction.
- (4) Projectiles with $L/D \leq 1/8$ show considerable flexure in which the central radial region of the penetrator temporarily loses contact with the target surface during penetration.
- (5) Absolute penetration decreases with decreasing L/D for constant diameter penetrators.
- (6) P/L increases with decreasing L/D , BUT ONLY UP TO A POINT (in this case, to an L/D ratio of approximately $1/8$). Beyond that, there is a decrease in P/L with decreasing L/D . This decrease can be related to the transition from rod mechanics to plate mechanics in the projectile.

INTENTIONALLY LEFT BLANK.

6. REFERENCES

- Bauer, D. P., and M. D. Nagy. "Operation Manual for 50-mm Research Gun System." UDR-TR-79-80, University of Dayton Research Institute, Dayton, OH, October 1979.
- Benck, R. F., and J. Robitaille. "Tensile Stress-Strain Curves III, Rolled Homogeneous Armor at a Strain Rate of 0.42 s⁻¹." BRL-MR-2760, U.S. Army Ballistic Research Laboratory, Aberdeen Proving Ground, MD, July 1977.
- Charters, A. C., and D. L. Orphal. "The Segmented Rod: A New Concept for the Defeat of Advanced Armor." Journal of Defense Research, 1989.
- Charters, A. C. "The Penetration of Rolled Homogeneous Armor by Continuous and Segmented Rods at High Velocity: Theory and Experiment." CR-87-1008, General Research Corporation, DARPA order No. 5070, 1987.
- Charters, A. C., T. L. Menna, and A. J. Piekutowski. "Penetration Dynamics of Rods From Direct Ballistic Tests of Advanced Armor Components at 2-3 km/s." International Journal of Impact Engineering, vol. 10, no. 1-4, pp. 93-106, December 1989.
- Christman, D. R., and J. W. Gehring. "Analysis of High-Velocity Projectile Penetration Mechanics." Journal of Applied Physics, vol. 37, no. 4, 1966.
- Cline, C. F., R. P. Gogolewski, and J. E. Reaugh. "Low Fineness Ratio Kinetic Energy Projectiles." Proceedings of the 11th International Symposium on Ballistics, Brussels, Belgium, 1987.
- Cuadros, J. H. "Monolithic and Segmented Projectile Penetration Experiments in the 2 to 4 Kilometers Per Second Impact Velocity Regime." International Journal of Impact Engineering, vol. 10, no. 1-4, pp. 147-157, December 1989.
- Denardo, B. P. "Projectile Shape Effects on Hypervelocity Impact Craters in Aluminum." TND-4953, NASA, Ames Report, 1989.
- Frank, K., and J. Zook. "Chunky Metal Penetrators Act Like Constant Mass Penetrators." Proceedings of the 12th International Symposium on Ballistics." San Antonio, TX, November 1990.
- Hauver, G. E., and A. Melani. "Behavior of Segmented Rods During Penetration." BRL-TR-3129, U.S. Army Ballistic Research Laboratory, Aberdeen Proving Ground, MD, July 1990.
- Herbette, G. "The Influence of Projectile Shape on Penetration Power." Proceedings of the 11th International Symposium on Ballistics, Brussels, Belgium, 1989.
- Hohler, V., and A. J. Stilp. "Hypervelocity Impact of Rod Projectiles with L/D from 1 to 32." International Journal of Impact Engineering, vol. 5, 1987.

- Hohler, V., and A. J. Stilp. "Penetration Performance of Segmented Rods at Different Spacing-Comparison With Homogeneous Rods at 2.5–3.5 km/s." Proceedings of the 12th International Symposium on Ballistics, San Antonio, TX, November 1990.
- Holland, P. M., J. T. Gordon, T. L. Menna, and A. C. Charters. "Hydrocode Results for the Penetration of Continuous, Segmented and Hybrid Rods Compared With Ballistic Experiments." International Journal of Impact Engineering, vol. 10, no. 1–4, pp. 241–250, December 1989.
- Hunkler, R. "Numerical Simulation of Segmented Rods." Proceedings of the 12th International Symposium on Ballistics, San Antonio, TX, November 1990.
- Johnson, W. Impact Strength of Materials. London: Edward Arnold 1972.
- Johnson, G. R. "EPIC-2, A Computer Program for Elastic-Plastic Impact Calculations in Two Dimensions Plus Spin." BRL-CR-00373, U.S. Army Ballistic Research Laboratory, Aberdeen Proving Ground, MD, June 1978.
- Kimsey, K. D., and J. A. Zukas. "Contact Surface Erosion for Hypervelocity Impact Problems." BRL-MR-3495, U.S. Army Ballistic Laboratory, Aberdeen Proving Ground, MD, February 1986.
- Kivity, Y., E. Yitzhak, and E. Hirsch. "Penetration of Segmented Rods into Homogeneous Targets." Proceedings of the 11th International Symposium on Ballistics, Brussels, Belgium, 1989.
- Kohn, B. J. "Compilation of Hugoniot Equations of State." AFWL-TR-69-38, Air Force Weapons Laboratory, 1969.
- McGlaun, J. M., and S. L. Thompson. "CTH: A Three-Dimensional Shock Wave Physics Code." International Journal of Impact Engineering, vol. 10, pp. 351–360, 1990.
- Naz, P., and H. F. Lehr. "The Crater Formation Due to Segmented Rod Penetrators." Proceedings of the 1989 Hypervelocity Impact Symposium, San Antonio, TX, December 1989.
- Nicholas, T. "Dynamic Tensile Testing of Structural Materials Using a Split Hopkinson Bar Apparatus." TR-80-4053, Air Force Wright Aeronautical Laboratories, Wright-Patterson AFB, OH, October 1980.
- Orphal, D. L., C. E. Anderson, and R. R. Franzen. "Impact Calculations of $L/D \leq 1$ Penetrators." Proceedings of the 12th International Symposium on Ballistics, San Antonio, TX, November 1990.
- Orphal, D. L., and R. R. Franzen. "Penetration Mechanics and Performance of Segmented Rods Against Metal Targets." International Journal of Impact Engineering, vol. 10, no. 1–4, December 1989.

- Raatschen, H. J., W. Pavel, S. Fuchs, H. Senf, and H. Rothenhausler. "Penetration Efficiency of Segmented Rods." Proceedings of the 11th International Symposium on Ballistics, Brussels, Belgium, 1987.
- Rinehart, J. S. Stress Transients in Solids. Santa Fe, NM: Hyperdynamics, 1975.
- Scheffler, D. R. "2-D Computer Simulations of Segmented Penetrators Impacting Semi-Infinite Steel Targets." International Journal of Impact Engineering, vol. 9, March 1989.
- Scheffler, D. R. and J. A. Zukas. "Numerical Simulation of Segmented Penetrator Impact." International Journal of Impact Engineering, vol. 10, no. 1-4, pp. 487-498, December 1989.
- Silsby, G. F., R. J. Roszak, and L. Giglio-Tos. "BRL's 50 mm High Pressure Powder Gun for Terminal Ballistic Testing - The First Year's Experience." BRL-MR-03236, U.S. Army Ballistic Research Laboratory, Aberdeen Proving Ground, MD, January 1983.
- Sorensen, B. R., K. D. Kimsey, G. F. Silsby, D. R. Scheffler, T. M. Sherrick, and W. S. de Rosset. "High Velocity Penetration of Steel Targets." International Journal of Impact Engineering, vol. 11, no. 1, 1991.
- Tate, A. "Engineering Modelling of Some Aspects of Segmented Rod Penetration." International Journal of Impact Engineering, vol. 9, no. 3, 1990.
- Wasley, R. J. Stress Wave Propagation in Solids: An Introduction. New York: Marcel Dekker, 1973.
- Zukas, J. A. "Numerical Simulation of Semi-Infinite Target Penetration by Continuous and Segmented Rods." BRL-TR-3081, U.S. Army Ballistic Research Laboratory, Aberdeen Proving Ground, MD, February 1990a.
- Zukas, J. A., ed. High Velocity Impact Dynamics. New York: Wiley Interscience, 1990b.
- Zukas, J. A., T. Nicholas, L. B. Greszczuk, H. F. Swift, and D. R. Curran. Impact Dynamics. New York: Wiley Interscience, 1982.
- Zukas, J. A., and S. B. Segletes. "Impact Response Calculations With Microcomputers." 10th International Conference on Structural Mechanics in Reactor Technology, Volume B: Computational Mechanics, American Association for Structural Mechanics in Reactor Technology, Los Angeles, CA, 1989.

INTENTIONALLY LEFT BLANK.

APPENDIX A:
L/D 1 SMASH INPUT DECK

INTENTIONALLY LEFT BLANK.

120 0 1 1 15000.

7.8	17.6	2.785
1.00E+20	1.00E+20	1.00E+20
7.78E+11	1.28E+12	2.60E+11
0.0	0.0	0.0
7.00E+09	14.3E+09	2.9E+09
7.00E+09	19.0E+09	2.9E+09
0.01	0.10	0.40
3.50E+10	2.00E+10	2.00E+10
1.019E+12	3.021E+12	0.76762E+12
4.220E+12	4.699E+12	1.28312E+12
5.129E+12	3.350E+12	1.25133E+12
1.69	1.43	2.00
0.10	0.10	0.10
2.00	2.00	2.00
1.00	1.00	1.0
1.00	1.00	1.00
2.2	2.2	2.20
21.	21.	21.

1 0 0 0
1.0 1.0 0. 0.0 0.00

6 1 14 27 2.54 0.0 1.270 0.0 1.0 1.0

1.0 1.0 0.0 0.0 0.0

6 1001 61 101 0.0 -10. 6.00 0.0 1.000 1.0

6 1 13 26 1 2

6 1001 60 100 2001 1

40 22 -1 2

2 1

14 742 28

741 729 -1

1001 1022 1

0.0 -2.00E+05

1.0E-10 1.0E-07 1.0E-11 0.6 80.E-06

0.E-06 1111. 1111. 0.0 1

5.0E-06 1111. 1111. 0.0 1

10.E-06 1111. 1111. 0.0 1

15.E-06 1111. 1111. 0.0 1

20.E-06 1111. 1111. 0.0 1

30.E-06 1111. 1111. 0.0 1

40.E-06 1111. 1111. 0.0 1

50.E-06 1111. 1111. 0.0 1

60.E-06 1111. 1111. 0.0 1

80.E-06 1111. 1111. 0.0 1

800.E-06 1111. 1111. 0.0 1

900.E-06 1111. 1111. 0.0 1

1000.E-06 1111. 1111. 0.0 1

1100.E-06	1111.	1111.	0.0	1
1200.E-06	1111.	1111.	0.0	1
1400.E-06	1111.	1111.	0.0	1
1600.E-06	1111.	1111.	0.0	1
1.0				

APPENDIX B:
L/D 1/2 SMASH INPUT DECK

INTENTIONALLY LEFT BLANK.

```

120 0 1 1 15000.
  7.8      17.6      2.785
  1.00E+20  1.00E+20  1.00E+20
  7.78E+11  1.28E+12  2.60E+11
  0.0       0.0      0.0
  7.00E+09  14.3E+09  2.9E+09
  7.00E+09  19.0E+09  2.9E+09
  0.01      0.10     0.40
  3.50E+10  2.00E+10  2.00E+10
  1.019E+12 3.021E+12 0.76762E+12
  4.220E+12 4.699E+12 1.28312E+12
  5.129E+12 3.350E+12 1.25133E+12
  1.69      1.43     2.00
  0.10      0.10     0.10
  2.00      2.00     2.00
  1.00      1.00     1.0
  1.00      1.00     1.00
  2.2       2.2      2.20
  21.       21.      21.
  1 0 0 0
1.0 1.0 0. 0.0 0.00

  6 1 14 14 1.27 0.0 1.270 0.0 1.0 1.0

1.0 1.0 0.0 0.0 0.0

  6 1001 61 101 0.0 -10. 6.00 0.0 1.000 1.0

  6 1 13 13 1 2

  6 1001 60 100 2001 1
27 22 -1 2
  2 1
14 378 28
377 365 -1
1001 1022 1
  0.0 -2.00E+05
  1.0E-10 1.0E-07 1.0E-11 0.6 80.E-06
  0.E-06 1111. 1111. 0.0 1
  5.0E-06 1111. 1111. 0.0 1
  10.E-06 1111. 1111. 0.0 1
  15.E-06 1111. 1111. 0.0 1
  20.E-06 1111. 1111. 0.0 1
  30.E-06 1111. 1111. 0.0 1
  40.E-06 1111. 1111. 0.0 1
  50.E-06 1111. 1111. 0.0 1
  60.E-06 1111. 1111. 0.0 1
  80.E-06 1111. 1111. 0.0 1
  800.E-06 1111. 1111. 0.0 1
  900.E-06 1111. 1111. 0.0 1
  1000.E-06 1111. 1111. 0.0 1

```

1100.E-06	1111.	1111.	0.0	1
1200.E-06	1111.	1111.	0.0	1
1400.E-06	1111.	1111.	0.0	1
1600.E-06	1111.	1111.	0.0	1
1.0				

APPENDIX C:
L/D 1/4 SMASH INPUT DECK

INTENTIONALLY LEFT BLANK.

120 0 1 1 15000.

7.8	17.6	2.785
1.00E+20	1.00E+20	1.00E+20
7.78E+11	1.28E+12	2.60E+11
0.0	0.0	0.0
7.00E+09	14.3E+09	2.9E+09
7.00E+09	19.0E+09	2.9E+09
0.01	0.10	0.40
3.50E+10	2.00E+10	2.00E+10
1.019E+12	3.021E+12	0.76762E+12
4.220E+12	4.699E+12	1.28312E+12
5.129E+12	3.350E+12	1.25133E+12
1.69	1.43	2.00
0.10	0.10	0.10
2.00	2.00	2.00
1.00	1.00	1.0
1.00	1.00	1.00
2.2	2.2	2.20
21.	21.	21.

1	0	0	0
1.0	1.0	0.	0.0 0.00

6	1	14	8	0.635	0.0	1.270	0.0	1.0	1.0
---	---	----	---	-------	-----	-------	-----	-----	-----

1.0	1.0	0.0	0.0	0.0
-----	-----	-----	-----	-----

6	1001	61	101	0.0	-10.	10.0	0.0	1.000	1.0
---	------	----	-----	-----	------	------	-----	-------	-----

6	1	13	7	1	2
---	---	----	---	---	---

6	1001	60	100	2001	1
21	22	-1	2		
2	1				
14	210	28			
209	197	-1			
1001	1022	1			
0.0	-2.00E+05				
1.0E-10	1.0E-07	1.0E-11	0.6	80.E-06	
0.E-06	1111.	1111.	0.0	1	
5.0E-06	1111.	1111.	0.0	1	
10.E-06	1111.	1111.	0.0	1	
15.E-06	1111.	1111.	0.0	1	
20.E-06	1111.	1111.	0.0	1	
30.E-06	1111.	1111.	0.0	1	
40.E-06	1111.	1111.	0.0	1	
50.E-06	1111.	1111.	0.0	1	
60.E-06	1111.	1111.	0.0	1	
80.E-06	1111.	1111.	0.0	1	
800.E-06	1111.	1111.	0.0	1	
900.E-06	1111.	1111.	0.0	1	
1000.E-06	1111.	1111.	0.0	1	

1100.E-06	1111.	1111.	0.0	1
1200.E-06	1111.	1111.	0.0	1
1400.E-06	1111.	1111.	0.0	1
1600.E-06	1111.	1111.	0.0	1
1.0				

APPENDIX D:
L/D 1/8 SMASH INPUT DECK

INTENTIONALLY LEFT BLANK.

```

120 0 1 1 15000.
    7.8    17.6    2.785
    1.00E+20    1.00E+20    1.00E+20
    7.78E+11    1.28E+12    2.60E+11
    0.0    0.0    0.0
    7.00E+09    14.3E+09    2.9E+09
    7.00E+09    19.0E+09    2.9E+09
    0.01    0.10    0.40
    3.50E+10    2.00E+10    2.00E+10
    1.019E+12    3.021E+12    0.76762E+12
    4.220E+12    4.699E+12    1.28312E+12
    5.129E+12    3.350E+12    1.25133E+12
    1.69    1.43    2.00
    0.10    0.01    0.10
    2.00    2.00    2.00
    1.00    1.00    1.0
    1.00    1.00    1.00
    2.2    2.2    2.20
    21.    21.    21.
1 0 0 0
1.0 1.0 0. 0.0 0.00

6 1 41 11 .3175 0.0 1.270 0.0 1.0 1.0

1.0 1.0 0.0 0.0 0.0

6 1001 61 101 0.0 -10. 6.00 0.0 1.000 1.0

6 1 40 10 1 2

6 1001 60 100 2001 1
51 22 -1 2
2 1
41 861 82
860 821 -1
1001 1022 1
0.0 -2.00E+05
1.0E-10 1.0E-07 1.0E-11 0.6 80.E-06
0.E-06 1111. 1111. 0.0 1
5.0E-06 1111. 1111. 0.0 1
10.E-06 1111. 1111. 0.0 1
15.E-06 1111. 1111. 0.0 1
20.E-06 1111. 1111. 0.0 1
30.E-06 1111. 1111. 0.0 1
40.E-06 1111. 1111. 0.0 1
50.E-06 1111. 1111. 0.0 1
60.E-06 1111. 1111. 0.0 1
80.E-06 1111. 1111. 0.0 1
800.E-06 1111. 1111. 0.0 1
900.E-06 1111. 1111. 0.0 1
1000.E-06 1111. 1111. 0.0 1

```

1100.E-06	1111.	1111.	0.0	1
1200.E-06	1111.	1111.	0.0	1
1400.E-06	1111.	1111.	0.0	1
1600.E-06	1111.	1111.	0.0	1
1.0				

APPENDIX E:
L/D 1/16 SMASH INPUT DECK

INTENTIONALLY LEFT BLANK.

```

120 0 1 1 72000.
  7.8      17.6      2.785
1.00E+20   1.00E+20   1.00E+20
7.78E+11   1.28E+12   2.60E+11
0.0        0.0        0.0
7.00E+09   14.3E+09   2.9E+09
7.00E+09   19.0E+09   2.9E+09
0.01       0.10      0.40
3.50E+10   2.00E+10   2.00E+10
1.019E+12   3.021E+12   0.76762E+12
4.220E+12   4.699E+12   1.28312E+12
5.129E+12   3.350E+12   1.25133E+12
1.69       1.43      2.00
0.10       0.10      0.10
2.00       2.00      2.00
999.       999.      1.0
1.00       1.00      1.00
2.2        2.2       2.20
21.        21.       21.
1 0 0 0
1.0 1.0 0. 0.0 0.00

6 1 85 11 .15875 0.0 1.270 0.0 1.0 1.0

1.0 1.0 0.0 0.0 0.0

6 2001 79 79 0.0 -6.0 6.00 0.0 1.000 1.0

6 1 84 10 1 2

6 2001 78 78 3401 1
95 22 -1 2
2 1
85 1785 170
1784 1701 -1
2001 2022 1
0.0 -2.00E+05
1.0E-10 1.0E-07 1.0E-11 0.6 100.E-06
0.E-06 1111. 1111. 0.0 1
5.0E-06 1111. 1111. 0.0 1
10.E-06 1111. 1111. 0.0 1
15.E-06 1111. 1111. 0.0 1
20.E-06 1111. 1111. 0.0 1
25.E-06 1111. 1111. 0.0 1
30.E-06 1111. 1111. 0.0 1
40.E-06 1111. 1111. 0.0 1
100.E-06 1111. 1111. 0.0 1
200.E-06 1111. 1111. 0.0 1
300.E-06 1111. 1111. 0.0 1
500.E-06 1111. 1111. 0.0 1
1000.E-06 1111. 1111. 0.0 1

```

1100.E-06	1111.	1111.	0.0	1
1200.E-06	1111.	1111.	0.0	1
1400.E-06	1111.	1111.	0.0	1
1600.E-06	1111.	1111.	0.0	1
1.0				

APPENDIX F:
L/D 1/32 SMASH INPUT DECK

INTENTIONALLY LEFT BLANK.

120 0 1 1 72000.

7.8	17.6	2.785
1.00E+20	1.00E+20	1.00E+20
7.78E+11	1.28E+12	2.60E+11
0.0	0.0	0.0
7.00E+09	14.3E+09	2.9E+09
7.00E+09	19.0E+09	2.9E+09
0.01	0.10	0.40
3.50E+10	2.00E+10	2.00E+10
1.019E+12	3.021E+12	0.76762E+12
4.220E+12	4.699E+12	1.28312E+12
5.129E+12	3.350E+12	1.25133E+12
1.69	1.43	2.00
0.10	0.10	0.10
2.00	2.00	2.00
999.	999.	1.0
1.00	1.00	1.00
2.2	2.2	2.20
21.	21.	21.

1	0	0	0
1.0	1.0	0.	0.0 0.00

6	1	85	11	.079375	0.0	1.270	0.0	1.0	1.0
---	---	----	----	---------	-----	-------	-----	-----	-----

1.0	1.0	0.0	0.0	0.0
-----	-----	-----	-----	-----

6	2001	61	101	0.0	-10.	10.0	0.0	1.000	1.0
---	------	----	-----	-----	------	------	-----	-------	-----

6	1	84	10	1	2
---	---	----	----	---	---

6	2001	60	100	3401	1
---	------	----	-----	------	---

95	22	-1	2
----	----	----	---

2	1
---	---

85	1785	170
----	------	-----

1784	1701	-1
------	------	----

2001	2022	1
------	------	---

0.0	-2.00E+05
-----	-----------

1.0E-10	1.0E-07	1.0E-11	0.6	100.E-06
---------	---------	---------	-----	----------

0.E-06	1111.	1111.	0.0	1
--------	-------	-------	-----	---

5.0E-06	1111.	1111.	0.0	1
---------	-------	-------	-----	---

10.E-06	1111.	1111.	0.0	1
---------	-------	-------	-----	---

15.E-06	1111.	1111.	0.0	1
---------	-------	-------	-----	---

20.E-06	1111.	1111.	0.0	1
---------	-------	-------	-----	---

25.E-06	1111.	1111.	0.0	1
---------	-------	-------	-----	---

30.E-06	1111.	1111.	0.0	1
---------	-------	-------	-----	---

40.E-06	1111.	1111.	0.0	1
---------	-------	-------	-----	---

100.E-06	1111.	1111.	0.0	1
----------	-------	-------	-----	---

200.E-06	1111.	1111.	0.0	1
----------	-------	-------	-----	---

300.E-06	1111.	1111.	0.0	1
----------	-------	-------	-----	---

500.E-06	1111.	1111.	0.0	1
----------	-------	-------	-----	---

1000.E-06	1111.	1111.	0.0	1
-----------	-------	-------	-----	---

1100.E-06	1111.	1111.	0.0	1
1200.E-06	1111.	1111.	0.0	1
1400.E-06	1111.	1111.	0.0	1
1600.E-06	1111.	1111.	0.0	1
1.0				

APPENDIX G:
L/D 1 CTH INPUT DECK

INTENTIONALLY LEFT BLANK.

```

*
*eor* cgenin
*
cth l/d=1 wa impacting rha at 2km/s
*
control
  ep
  mmp
* usessd
endcontrol
convct
  convection 1
  interface high
endc
*
mesh
  block 1 geom 2dc type e
    x0 0.
    x1 n 150 dxf 0.1058332 rat 1.0
    endx
    y0 -3.598332
    y1 n 200 dyf=.1058332 rat 1.0
    endy
    xact 0.0 2.0
    yact -3.0 1.0
  endblock
endmesh
*
insertion of material
  block 1
    package 'target'
    material 1
    numsub 25
    insert box
      x1 0.0 x2 1000.0
      y1 0.0 y2 1000.0
    endinsert
  endpackage
  package 'rod'
  material 2
  numsub 25
  velocities yvel 2.0e5
  insert box
    x1 0.0 x2 1.27
    y1 -2.54 y2 0.0
  endinsert
  endpackage
endblock
endinsertion
*
edit
  block 1
    expanded

```

```

endblock
endedit
*
eos num 2
mat1 -1
mat2 -2
  aneos -1 iron    rhug=-1 thug=-1
  aneos1 1 -1 7.86 0. 0. 4.5e5 1.69 0.
  aneos1 3.1416 0. -1. -7.36e10 0. 0. 0.
  aneos1 0. 0. 0. 0. 0. 0. 0.
  aneos1 26 1.
  aneos1 -2 tungsten rhug=-1 thug=-1
  aneos2 3 -1 17.3 0. 0. 4.0e5 1.43 0.
  aneos3 1.295 0. -1. -4.52e10 0. 0. 0.
  aneos4 0. 0. 0. 0. 0. 0. 0.
  aneos5 74. .9
  aneos6 28 .07
  aneos7 26 .03
endeos
*
tracer
  block 1
  add 0.0 -0.15
  add 0.0 -2.35
endtracer
*
endinput
*
*eor* cthin
cth l/d=1 wa impacting rha at 2km/s
*
control
  mmp
  tstop 10.0e-05
  cpshift 999.
  rdumpf=14400.
* pvoid 10.0
* usessd
endcontrol
*
edit
  shortt
  time 0. dtfrequency 1.0e-06
  ends
  longt
  time 0. dtfrequency 1.0e-05
  endl
  plott
  time 0. dtfrequency 1.0e-05
  endp
  histt
  time 0. dtfrequency 1.0e-07
  time 1.0e-05 dtfrequency 1.0e-06

```

```

        htracer1
        htracer2
    endh
ende
*
boundary
    bhydro
        block 1
            bxbot 0
            bxtop 1
            bybot 1
            bytop 1
        endb
    endh
endb
*
epdata
    matep 1 yield 7.0e9 poisson 0.33
    matep 2 yield 19.3e9 poisson 0.30
    mix 3
ende
*
fracts
    pressure
        pfmix -30.0e9
        pfvoid -30.0e9
        pfrac1 -35.0e9
        pfrac2 -20.0e9
    endf
*

```


INTENTIONALLY LEFT BLANK.

APPENDIX H:
L/D 1/2 CTH INPUT DECK

INTENTIONALLY LEFT BLANK.

```

*
*eor* cgenin
*
cth l/d=.50 wa impacting rha at 2kn/s
*
control
  ep
  mmp
* usessd
endcontrol
convct
  convection 1
  interface high
endc
*
mesh
  block 1 geom 2dc type e
    x0 0.
    x1 n 300 dxf 0.0529166 rat 1.0
    endx
    y0 -3.069166
    y1 n 224 dyf=.0529166 rat 1.0
    y2 n 20 dyf=.0529166 rat 1.05
    endy
    xact 0.0 2.0
    yact -1.5 1.0
  endblock
endmesh
*
insertion of material
  block 1
    package 'target'
    material 1
    numsub 25
    insert box
      x1 0.0 x2 1000.0
      y1 0.0 y2 1000.0
    endinsert
  endpackage
  package 'rod'
  material 2
  numsub 25
  velocities yvel 2.0e5
  insert box
    x1 0.0 x2 1.27
    y1 -1.27 y2 0.0
  endinsert
  endpackage
endblock
endinsertion
*
edit
  block 1

```

```

expanded
endblock
endedit
*
eos num 2
mat1 -1
mat2 -2
  aneos -1 iron rhug=-1 thug=-1
  aneos1 1 -1 7.86 0. 0. 4.5e5 1.69 0.
  aneosi 3.1416 0. -1. -7.36e10 0. 0. 0.
  aneosi 0. 0. 0. 0. 0. 0. 0.
  aneosi 26 1.
  aneos1 -2 tungsten rhug=-1 thug=-1
  aneos2 3 -1 17.3 0. 0. 4.0e5 1.43 0.
  aneos3 1.295 0. -1. -4.52e10 0. 0. 0.
  aneos4 0. 0. 0. 0. 0. 0. 0.
  aneos5 74. .9
  aneos6 28 .07
  aneos7 26 .03

```

```

endeos

```

```

*
tracer
  block 1
  add 0.0 -0.05
  add 0.0 -1.26
endtracer

```

```

*
endinput

```

```

*eor* cthin
cth l/d=.5 wa impacting rha at 2km/s

```

```

control
  nimp
  tstop 10.0e-05
  cpshift 999.
  rdumpi=14400.
* pvoid 10.0
* usesd
endcontrol

```

```

edit
  shortt
    time 0. dtfrequency 1.0e-06
  ends
  longt
    time 0. dtfrequency 1.0e-05
  endl
  plott
    time 0. dtfrequency 1.0e-05
  endp
  histt
    time 0. dtfrequency 1.0e-07

```

```

time 1.0e-05 dtfrequency 1.0e-06
  htracer1
  htracer2
endh
ende
*
boundary
  bhydro
    block 1
      bxbot 0
      bxtop 1
      bybot 1
      bytop 1
    endb
  endh
endb
*
epdata
  matep 1 yield 7.0e9 poisson 0.33
  matep 2 yield 19.3e9 poisson 0.30
  mix 3
ende
*
fracts
  pressure
    pfmix -30.0e9
    pfvoid -30.0e9
    pfrac1 -35.0e9
    pfrac2 -20.0e9
  endf
  *

```

INTENTIONALLY LEFT BLANK.

APPENDIX I:
L/D 1/4 CTH INPUT DECK

INTENTIONALLY LEFT BLANK.

```

*
*eor* cgenin
*
cth l/d=.250 wa impacting rha at 2km/s
*
control
  ep
  mmp
* usessd
endcontrol
convct
  convection 1
  interface high
endc
*
mesh
block 1 geom 2dc type e
  x0 0.
  x1 n 300 dxf 0.0529166 rat 1.0
  endx
  y0 -1.2699984
  y1 n 224 dyf=.0529166 rat 1.0
  endy
  xact 0.0 2.0
  yact -1.0 1.0
endblock
endmesh
*
insertion of material
block 1
  package 'target'
  material 1
  numsub 25
  insert box
    x1 0.0 x2 1000.0
    y1 0.0 y2 1000.0
  endinsert
  endpackage
  package 'rod'
  material 2
  numsub 25
  velocities yvel 2.0e5
  insert box
    x1 0.0 x2 1.27
    y1 -.635 y2 0.0
  endinsert
  endpackage
endblock
endinsertion
*
edit
block 1
  expanded

```

```

endblock
endedit
*
eos num 2
mat1 -1
mat2 -2
  aneos -1 iron rhug=-1 thug=-1
  aneos1 1 -1 7.86 0. 0. 4.5e5 1.69 0.
  aneosi 3.1416 0. -1. -7.36e10 0. 0. 0.
  aneosi 0. 0. 0. 0. 0. 0. 0.
  aneosi 26 1.
  aneos1 -2 tungsten rhug=-1 thug=-1
  aneos2 3 -1 17.3 0. 0. 4.0e5 1.43 0.
  aneos3 1.295 0. -1. -4.52e10 0. 0. 0.
  aneos4 0. 0. 0. 0. 0. 0. 0.
  aneos5 74. .9
  aneos6 28 .07
  aneos7 26 .03
endeos
*
tracer
  block 1
  add 0.0 -0.01
  add 0.0 -0.634
  add 0.0 -0.3175
endtracer
*
endinput
*
*eor* cthin
cth l/d=.25 wa impacting rha at 2km/s
*
control
  mmp
  tstop 10.0e-05
  cpshift 999.
  rdumpf=14400.
* pvoid i0.0
* usessd
endcontrol
*
edit
  shortt
  time 0. dtfrequency 1.0e-06
  ends
  longt
  time 0. dtfrequency 1.0e-05
  endl
  plott
  time 0. dtfrequency 1.0e-05
  endp
  histt
  time 0. dtfrequency 0.05e-06

```

```

time 2.0e-06 dtfrequency 0.1e-06
time 10.e-06 dtfrequency 1.0e-06
  htracer1
  htracer2
  htracer3
endh
ende
*
boundary
  bhydro
    block 1
      bxbot 0
      bxtop 1
      bybot 1
      bytop 1
    endb
  eridh
endb
*
epdata
  matep 1 yield 7.0e9 poisson 0.33
  matep 2 yield 19.3e9 poisson 0.30
  mix 3
ende
*
fracts
  pressure
    pfmix -30.0e9
    pfvoid -30.0e9
    pfrac1 -35.0e9
    pfrac2 -20.0e9
endf
*

```

INTENTIONALLY LEFT BLANK.

APPENDIX J:
L/D 1/8 CTH INPUT DECK

INTENTIONALLY LEFT BLANK.

```

*
*eor* cgenin
*
cth Vd=.125 (1/8 wa impacting rha at 2km/s
*
control
  ep
  mmp
* usessd
endcontrol
convct
  convection 1
  interface high
endc
*
mesh
  block 1 geom 2dc type e
    x0 0.
    x1 n 300 dxf 0.03175 rat 1.0
    endx
    y0 -.47625
    y1 n 320 dyf=.03175 rat 1.0
    endy
    xact 0.0 2.0
    yact -.5 .5
  endblock
endmesh
*
insertion of material
  block 1
    package 'target'
    material 1
    numsub 25
    insert box
      x1 0.0 x2 1000.0
      y1 0.0 y2 1000.0
    endinsert
  endpackage
  package 'rod'
  material 2
  numsub 25
  velocities yvel 2.0e5
  insert box
    x1 0.0 x2 1.27
    y1 -.3175 y2 0.0
  endinsert
  endpackage
endblock
endinsertion
*
edit
  block 1
    expanded

```



```

endblock
endedit
*
eos num 2
mat1 -1
mat2 -2
  aneos -1 iron rhug=-1 thug=-1
  aneosi 1 -1 7.86 0. 0. 4.5e5 1.69 0.
  aneosi 3.1416 0. -1. -7.36e10 0. 0. 0.
  aneosi 0. 0. 0. 0. 0. 0. 0.
  aneosi 26 1.0
  aneosw -2 tungsten rhug=-1 thug=-1
  aneosw 3 -1 17.3 0. 0. 4.0e5 1.43 0.
  aneosw 1.295 0. -1. -4.52e10 0. 0. 0.
  aneosw 0. 0. 0. 0. 0. 0. 0.
  aneosw 74. .9
  aneosw 28 .07
  aneosw 26 .03
endeos
*
tracer
  block 1
  add 0.0 -0.01
  add 0.0 -0.3174
  add 0.0 -0.15875
endtracer
*
endinput
*
*eor* cthin
cth 1/d=.125 (1/8) wa impacting rha at 2km/s
*
control
  mmp
  tstop 10.0e-05
  cpshitt 999.
  rdumpf=14400
* pvoid 10.0
* usessd
endcontrol
*
edit
  shortt
  time 0. dtfrequency 1.0e-06
  ends
  longt
  time 0. dtfrequency 1.0e-05
  endl
  plott
  time 0. dtfrequency 1.0e-05
  endp
  histt
  time 0. dtfrequency 0.05e-06

```

```

time 2.0e-06 dtfrequency 0.1e-06
time 10.0e-06 dtfrequency 1.0e-06
  htracer1
  htracer2
  htracer3
endh
ende
*
boundary
  bhydro
    block 1
      bxbot 0
      bxtop 1
      bybot 1
      bytop 1
    endb
  endh
endb
*
epdata
  matep 1 yield 7.0e9 poisson 0.33
  matep 2 yield 19.3e9 poisson 0.30
  mix 3
ende
*
fracts
  pressure
    pfmix -30.0e9
    pfvoid -30.0e9
    pfrac1 -35.0e9
    pfrac2 -20.0e9
  endf
  *

```

INTENTIONALLY LEFT BLANK.

APPENDIX K:
L/D 1/16 CTH INPUT DECK

INTENTIONALLY LEFT BLANK.

```

*
*eor* cgenin
*
cth l/d=.0625 (1/16) wa impacting rha at 2km/s
*
control
  ep
  * mmt
  * usessd
endcontrol
*
mesh
  block 1 geom 2dc type e
    x0 0.
    x1 n 300 dxf 0.015875 rat 1.0
    endx
    y0 -.3175
    y1 n 320 dyf=.015875 rat 1.0
    endy
    xact 0.0 2.0
    yact -.5 .5
  endblock
endmesh
*
insertion of material
  block 1
    package 'target'
    material 1
    numsub 25
    insert box
      x1 0.0 x2 1000.0
      y1 0.0 y2 1000.0
    endinsert
  endpackage
  package 'rod'
  material 2
  numsub 25
  velocities yvel 2.0e5
  insert box
    x1 0.0 x2 1.27
    y1 -.15875 y2 0.0
  endinsert
  endpackage
endblock
endinsertion
*
edit
  block 1
    expanded
  endblock
endedit
*
eos num 2

```

```

mat1 -1
mat2 -2
  aneos -1 iron rhug=-1 thug=-1
  aneosi 1 -1 7.86 0. 0. 4.5e5 1.69 0.
  aneosi 3.1416 0. -1. -7.36e10 0. 0. 0.
  aneosi 0. 0. 0. 0. 0. 0. 0.
  aneosi 26 1.0
  aneosw -2 tungsten rhug=-1 thug=-1
  aneosw 3 -1 17.3 0. 0. 4.0e5 1.43 0.
  aneosw 1.295 0. -1. -4.52e10 0. 0. 0.
  aneosw 0. 0. 0. 0. 0. 0. 0.
  aneosw 74. .9
  aneosw 28 .07
  aneosw 26 .03
endeos
*
endinput
*
*eor* cthin
cth l/d=.0625 (1/16) wa impacting rha at 2km/s
*
control
  tstop 8.0e-05
  cpshift 999.
  rdumpf=14400
* pvoid 10.0
* usessd
endcontrol
*
edit
  shortt
    time 0. dtfrequency 1.0e-06
  ends
  longt
    time 0. dtfrequency 1.0e-05
  endl
  plott
    time 0. dtfrequency 1.0e-05
  endp
  histt
    time 0. dtfrequency 1.0e-06
  endh
ende
*
boundary
  bhydro
    block 1
    bxbot 0
    bxtop 1
    bybot 1
    bytop 1
  endb
endh

```

```
endb
*
epdata
  matep 1 yield 7.0e9 poisson 0.33
  matep 2 yield 19.3e9 poisson 0.30
  mix 3
ende
*
fracts
  pressure
    pfmix -1.0e6
    pfvoid -1.0e6
    pfrac1 -20.0e9
    pfrac2 -30.0e9
  endf
*
```


INTENTIONALLY LEFT BLANK.

APPENDIX L:
L/D 1/32 CTH INPUT DECK

INTENTIONALLY LEFT BLANK.

```

*
*eor* cgenin
*
cth l/d=.03125 (1/32) wa impacting rha at 2km/s
*

control
  ep
  mmp
* usessd
endcontrol
*

mesh
  block 1 geom 2dc type e
    x0 0.
    x1 n 300 dx=.0079375 rat 1.0
    x2 n 75 dx=.0079375 rat 1.05
    endx
    y0 -.15875
    y1 n 320 dy=.0079375 rat 1.0
    y2 n 75 dy=.0079375 rat 1.05
    endy
    xact 0.0 2.0
    yact -.5 .5
  endblock
endmesh
*

insertion of material
  block 1
    package 'target'
    material 1
    numsub 25
    insert box
      x1 0.0 x2 1000.0
      y1 0.0 y2 1000.0
    endinsert
  endpackage
  package 'rod'
  material 2
  numsub 25
  velocities yvel 2.0e5
  insert box
    x1 0.0 x2 1.27
    y1 -.079375 y2 0.0
  endinsert
  endpackage
endblock
endinsertion
*

edit
  block 1
    expanded
  endblock
endedit

```

```

*
eos num 2
mat1 -1
mat2 -2
  aneos -1 iron   rhug=-1 thug=-1
  aneosi 1 -1 7.86 0. 0. 4.5e5 1.69 0.
  aneosi 3.1416 0. -1. -7.36e10 0. 0. 0.
  aneosi 0. 0. 0. 0. 0. 0. 0.
  aneosi 26 1.0
  aneosw -2 tungsten rhug=-1 thug=-1
  aneosw 3 -1 17.3 0. 0. 4.0e5 1.43 0.
  aneosw 1.295 0. -1. -4.52e10 0. 0. 0.
  aneosw 0. 0. 0. 0. 0. 0. 0.
  aneosw 74. .9
  aneosw 28 .07
  aneosw 26 .03
endeos
*
tracer
  block 1
  add 0.0 0.0
  add 0.0 -0.079375
  add 0.0 -0.0396875
endtracer
*
endinput
*
*eor* cthin
cth l/d=.03125 (1/32) wa impacting rha at 2km/s
*
control
  mmp
  tstop 50.0e-06
  cpshift 999.
  rdumpf=14400
* pvoid 10.0
* usessd
endcontrol
convct
  convection 1
  interface high
endc
*
*restart
* cycle=6644
*endrestart
*
edit
  shortt
  time 0. dtfrequency 1.0e-06
  ends
  longt
  time 0. dtfrequency 1.0e-05

```

```

endl
plott
  time 0. dtfrequency 1.0e-05
endp
histt
  time 0. dtfrequency 0.05e-06
  time 2.0e-06 dtfrequency 0.1e-06
  time 10.0e-06 dtfrequency 1.0e-06
  htracer1
  htracer2
  htracer3
endh
ende
*
boundary
  bhydro
    block 1
      bxbot 0
      bxtop 1
      bybot 1
      bytop 1
    endb
  endh
endb
*
epdata
  matep 1 yield 7.0e9 poisson 0.33
  matep 2 yield 19.3e9 poisson 0.30
  mix 3
ende
*
fracts
  pressure
    pfmix -30.0e9
    pfvoid -30.0e9
    pfrac1 -35.0e9
    pfrac2 -20.0e9
  endf
  *

```

INTENTIONALLY LEFT BLANK.

LIST OF SYMBOLS

- c - Material Acoustic Velocity
- c_p - Penetrator Material Acoustic Velocity
- c_t - Target Material Acoustic Velocity
- D - Penetrator Diameter
- E - Penetrator Kinetic Energy
- H - Penetration Channel Diameter
- L - Penetrator Length
- P - Penetration Channel Depth
- r - Target radial dimension
- t - Time
- v - Particle Velocity
- V_s - Impact Velocity
- ρ - Material Density
- ρ_p - Penetrator Material Density
- ρ_t - Target Material Density

INTENTIONALLY LEFT BLANK.

<u>No. of</u> <u>Copies</u>	<u>Organization</u>		<u>No. of</u> <u>Copies</u>	<u>Organization</u>
2	Administrator Defense Technical Info Center ATTN: DTIC-DDA Cameron Station Alexandria, VA 22304-6145		1	Commander U.S. Army Missile Command ATTN: AMSMI-RD-CS-R (DOC) Redstone Arsenal, AL 35898-5010
1	Commander U.S. Army Materiel Command ATTN: AMCDRA-ST 5001 Eisenhower Avenue Alexandria, VA 22333-0001		1	Commander U.S. Army Tank-Automotive Command ATTN: ASQNC-TAC-DIT (Technical Information Center) Warren, MI 48397-5000
1	Commander U.S. Army Laboratory Command ATTN: AMSLC-DL 2800 Powder Mill Road Adelphi, MD 20783-1145		1	Director U.S. Army TRADOC Analysis Command ATTN: ATRC-WSR White Sands Missile Range, NM 88001
2	Commander U.S. Army Armament Research, Development, and Engineering Center ATTN: SMCAR-IMI-I Picatinny Arsenal, NJ 07806-5000	(Class. only)1	1	Commandant U.S. Army Field Artillery School ATTN: ATSF-CSI Ft. Sill, OK 73503-5000
2	Commander U.S. Army Armament Research, Development, and Engineering Center ATTN: SMCAR-TDC Picatinny Arsenal, NJ 07806-5000	(Unclass. only)1		Commandant U.S. Army Infantry School ATTN: ATSH-CD (Security Mgr.) Fort Benning, GA 31905-5660
1	Director Benet Weapons Laboratory U.S. Army Armament Research, Development, and Engineering Center ATTN: SMCAR-CCB-TL Watervliet, NY 12189-4050		1	Air Force Armament Laboratory ATTN: WL/MNOI Eglin AFB, FL 32542-5000
(Unclass. only)1	Commander U.S. Army Armament, Munitions and Chemical Command ATTN: AMSMC-IMF-L Rock Island, IL 61299-5000			<u>Aberdeen Proving Ground</u>
1	Director U.S. Army Aviation Research and Technology Activity ATTN: SAVRT-R (Library) M/S 219-3 Ames Research Center Moffett Field, CA 94035-1000		2	Dir, USAMSAA ATTN: AMXSY-D AMXSY-MP, H. Cohen
			1	Cdr, USATECOM ATTN: AMSTE-TD
			3	Cdr, CRDEC, AMCCOM ATTN: SMCCR-RSP-A SMCCR-MU SMCCR-MSI
			1	Dir, VLAMO ATTN: AMSLC-VL-D
			10	Dir, BRL ATTN: SLCBR-DD-T

No. of	
<u>Copies</u>	<u>Organization</u>
2	Director DARPA ATTN: J. Richardson MAJ R. Lundberg 1400 Wilson Blvd. Arlington, VA 22209-2308
2	Commander U.S. Army MICOM ATTN: AMSMI-RD-TE-F, Matt H. Triplett Redstone Arsenal, AL 35898-5250
2	Commander U.S. Army Tank-Automotive Command ATTN: AMCPM-ABMS-SA, John Rowe AMSTA-RSS, K. D. Bishnoi Warren, MI 48397-5000
2	Commander U.S. Army Armament Research, Development, and Engineering Center ATTN: SMCAR-CCH-V, M. D. Nicolich SMCAR-FSA-E, W. P. Dunn Picatinny Arsenal, NJ 07806-5000
4	Commander U.S. Army Belvoir Research, Development, and Engineering Center ATTN: STRBE-NAE, Bryan Westlich STRBE-JMC, Terilee Hanshaw STRBE-NAN, Steven G. Bishop Josh Williams Fort Belvoir, VA 22060-5166
1	Commander U.S. Army Research Office P.O. Box 12211 Research Triangle Park, NC 27709-2211
1	Commander U.S. Army Foreign Science and Technology Center ATTN: AIAST-IS 220 Seventh Street, NE Charlottesville, VA 22901-5396

No. of	
<u>Copies</u>	<u>Organization</u>
1	Commander Det S, USAOG USAINSCOM ATTN: IAGPC-S Fort Meade, MD 20755
1	Director U.S. Army Missile and Space Intelligence Center ATTN: AIAMS-YDL Redstone Arsenal, AL 35898-5000
1	Commander, USACECOM R&D Technical Library ATTN: ASQNC-ELC-IS-L-R, Myer Center Fort Monmouth, NJ 07703-5000
5	Commander Naval Weapons Center ATTN: Code 3263, Tucker T. Yee Code 3268, Don Thompson Code 6214, W. J. McCarter Code 4057 Code 45, Tech Library China Lake, CA 93555-6001
3	Commander Naval Surface Warfare Center ATTN: Code G-22, Charles R. Garnett Code G-33, Linda F. Williams Code H-11, Mary Jane Sill Dahlgren, VA 22448-5000
2	Commander Naval Weapons Support Center ATTN: John D. Barber Sung Y. Kim Code 2024 Crane, IN 47522-5020
1	Officier-in-Charge Civil Engineering Laboratory Naval Construction Battalion Center ATTN: Code L-56, Joel Young Port Hueneme, CA 93041

No. of Copies	Organization	No. of Copies	Organization
18	<p>Commander Naval Surface Warfare Center ATTN: G-402, Pao C. Huang R-12, Bryan A. Baudler Robert H. Moffett Robert Garrett R-32, Thomas L. Jungling U-43, Richard Caminity R-10A, W. Reed John P. Matra Paula Walter Lisa Mensi Kenneth Kiddy F. J. Zerilli T. Spivok R. Phinney C. Smith E. Johnson W. Bullock C. Dickerson 10901 New Hampshire Ave. Silver Spring, MD 20903-5000</p>	1	<p>WRDC/MTX ATTN: Mr. Lee Kennard Wright-Patterson AFB, OH 45433</p>
		1	<p>Central Intelligence Agency Office of Central Reference Dissemination Branch Room GE-47 HQS Washington, DC 20502</p>
		1	<p>Advanced Technology, Inc. ATTN: John Adams P.O. Box 125 Dahlgren, VA 22448-0125</p>
1	<p>Commander Naval Surface Warfare Center ATTN: Code 730, Library Silver Spring, MD 20910</p>	16	<p>Director Sandia National Laboratories ATTN: Division 9122, Robert O. Nellums Jim Hickerson Division 1533, P. Yarrington Marlin Kipp Allen Robinson J. Stephen Rottler Division 2512, William J. Andrzejewski Don Marchi Division 1551, R. Graham R. Lafarge M. Vigil R. Sandoval J. Asay R. Longcope M. Forrestal Division 1541 J. McGlaun P.O. Box 5800 Albuquerque, NM 87185</p>
1	<p>Commander Naval EOD Technology Center ATTN: Code 6052A, C. Cherry Indian Head, MD 20640</p>		
1	<p>AFATL/DLJR ATTN: J. Foster Eglin AFB, FL 32542</p>		
4	<p>Air Force Armament Laboratory ATTN: AFATL/DLJW, W. Cook M. Nixon AFATL/MNW, LT Donald Lorey Richard D. Guba Eglin AFB, FL 32542</p>	1	<p>Explosive Technology ATTN: Michael L. Knaebel P.O. Box KK Fairfield, CA 94533</p>

No. of	
<u>Copies</u>	<u>Organization</u>
13	<p>Director Los Alamos National Laboratory ATTN: MS K574, G. E. Cort Tony Rollett Mike Burkett MS P940, Robert Karpp MS K557 N-6, Rudy Henninger MS G740, Roy Greiner B214 T-14, James P. Ritchie B216, J. W. Hopson MS F663, T. Adams MS G787, John Bolstad J. Walsh C. Mautz Tech Library P.O. Box 1663 Los Alamos, NM 87545</p>
14	<p>Director Lawrence Livermore National Laboratory ATTN: L-122, Barry R. Bowman Ward Dixon Raymond Pierce Russell Rosinsky Owen J. Alford Diana Stewart Tony Vidlak L-290, Albert Holt John E. Reaugh L-352, David Wood L-874, Robert M. Kuklo MS-35, Thomas McAbee Michael J. Murphy Technical Library P.O. Box 808 Livermore, CA 94550</p>
2	<p>Southwest Research Institute ATTN: C. Anderson A. Wenzel PO Drawer 28255 San Antonio, TX 78228-0255</p>

No. of	
<u>Copies</u>	<u>Organization</u>
3	<p>Battelle ATTN: R. Jameson S. Golaski TACTEC Library, J. N. Huggins 505 King Ave. Columbus, OH 43201-2693</p>
1	<p>Defense Technology International, Inc. ATTN: D. E. Ayer The Stark House 22 Concord Street Nashua, NH 03060</p>
3	<p>California Research and Technology, Inc. ATTN: Roland Franzen Dennis Orphal Ron E. Brown 5117 Johnson Drive Pleasanton, CA 94566</p>
1	<p>California Research and Technology, Inc. ATTN: Mark Majerus P.O. Box 2229 Princeton, NJ 08543</p>
1	<p>Rockwell Missile Systems Division ATTN: Terry Neuhart 1800 Satellite Blvd. Duluth, GA 30136</p>
1	<p>Rockwell Intl./Rocketdyne Division ATTN: James Moldenhauer 6633 Canoga Ave (HB 23) Canoga Park, CA 91303</p>
2	<p>McDonnell-Douglas Helicopter ATTN: Loren R. Bird Lawrence A. Mason 5000 E. McDowell Rd. (MS 543-D216) Mesa, AZ 85205</p>
1	<p>S-Cubed ATTN: Dr. R. T. Sedgwick P.O. Box 1620 La Jolla, CA 92083-1620</p>

No. of

Copies Organization

- 2 Orlando Technology, Inc.
ATTN: Dan Matuska
J. Osborn
P.O. Box 855
Shalimar, FL 32579
- 3 Kaman Sciences Corporation
ATTN: D. Barnette
D. Elder
P. Bussell
P.O. Box 7463
Colorado Springs, CO 80933-7463
- 2 Physics International Company
ATTN: Ron Funston
Lamont Garnett
2700 Merced St.
P.O. Box 5010
San Leandro, CA 94577
- 2 Lockheed Missile & Space Co., Inc.
ATTN: S. Kusumi (O-81-11, Bldg.157)
Jack Philips (O-54-50)
P.O. Box 3504
Sunnyvale, CA 94088
- 1 Lockheed Missile & Space Co., Inc.
ATTN: Richard A. Hoffman
Santa Cruz Facility
Empire Grade Road
Santa Cruz, CA 95060
- 2 Mason & Hanger - Silas Mason Co.
ATTN: Thomas J. Rowan
Christopher Vogt
Iowa Army Ammunition Plant
Middletown, IA 52638-9701
- 1 Lockheed Engineering & Space Sciences
ATTN: Ed Cykowski, MS B-22
2400 NASA Road 1
Houston, TX
- 2 Dyna East Corporation
ATTN: P. C. Chou
R. Ciccarelli
3201 Arch St.
Philadelphia, PA 19104

No. of

Copies Organization

- 2 E. I. DuPont De Nemours & Company
ATTN: B. Scott
L. Minor
Security Director, Legal Department
P.O. Box 1635
Wilmington, DE 19899
- 1 Aerojet Electro Systems Company
ATTN: Warhead Systems,
Dr. J. Carleone
P.O. Box 296
Azusa, CA 91702
- 1 Physics International Company
Tactical Systems Group
Eastern Division
P.O. Box 1004
Wadsworth, OH 44281-0904
- 3 Alliant Techsystems, Inc.
Defense Systems Division
ATTN: G. Johnson
J. Houlton
N. Berkholtz
7225 Northland Drive
Brooklyn Park, MN 55428
- 1 Martin Marietta Aerospace
ATTN: Donald R. Bragg
P.O. Box 5837, MP 109
Orlando, FL 32855
- 1 SRI International
ATTN: Dr. L. Seaman
333 Ravenswood Ave.
Menlo Park, CA 94025
- 1 Northrop Corporation
Electro-Mechanical Division
ATTN: Donald L. Hall
500 East Orangethorpe Ave.
Anaheim, CA 92801

No. of

Copies Organization

- 3 Boeing Aerospace Co.
Shock Physics & Applied Math
Engineering Technology
ATTN: R. Helzer
J. Shrader
T. Murray
P.O. Box 3999
Seattle, WA 98124
- 1 McDonnell Douglas Astronautics Company
ATTN: Bruce L. Cooper
5301 Bolsa Ave
Huntington Beach, CA 92647
- 1 D.R. Kennedy and Associates Inc.
ATTN: Donald Kennedy
P.O. Box 4003
Mountain View, CA 94040
- 1 University of Colorado
ATTN: Timothy Maclay
Campus Box 431, NNT 3-41
Boulder, CO 80309
- 1 New Mexico Institute Mining & Tech.
ATTN: David J. Chavez
Campus Station, TERA Group
Socorro, NM 87801

No. of	
<u>Copies</u>	<u>Organization</u>
2	Defense Research Establishment Suffield ATTN: Chris Weickert David Mackay Ralston, Alberta, TOJ 2N0 Ralston CANADA
1	Defense Research Establishment Valcartier ATTN: Norbert Gass P.O. Box 8800 Courcellette, PQ, GOA 1R0 CANADA
1	Canadian Arsenals, LTD ATTN: Pierre Pelletier 5 Montee des Arsenaux Ville de Gardeur, PQ, J5Z2 CANADA
3	IABG ATTN: H. J. Raatschen W. Schittke F. Scharppf Einsteinstrasse 20 D-8012 Ottobrun B. Muenchen GERMANY
1	Royal Armament R&D Establishment ATTN: Ian Cullis Fort Halstead Sevenoaks, Kent TN14 7BJ ENGLAND
1	Centre d'Etudes de Gramat ATTN: SOLVE Gerald 46500 Gramat FRANCE
1	Centre d'Etudes de Vaujours ATTN: PLOTARD Jean-Paul Boite Postale No. 7 77151 Country FRANCE
1	PRB S.A. ATTN: M. Vansnick Avenue de Tervueren 168, Bte. 7 Brussels, B-1150 BELGIUM

No. of	
<u>Copies</u>	<u>Organization</u>
2	AB Bofors/Ammunition Division ATTN: Jan Hasslid Anders Nordell BOX 900 S-691 80 Bofors SWEDEN
1	Messerschmitt-Bölkow-Blohm Dynamics Division ATTN: Manfred Held P.O. Box 1340 D-8898 Schrobenhausen GERMANY
1	TNO Prins Maurits Laboratory ATTN: H. J. Passman P.O. Box 45 2280 AA Rijswijk Lange Kleiweg 137 THE NETHERLANDS
1	ISL ATTN: CHANTERET Pierre-Yve F68301 Saint-Louis Cédex, 12, rue de l'Industrie B.P. 301 FRANCE
1	Lothar Meyer IFAM Lesumer Heerstrasse 36 Bremen 77 GERMANY

INTENTIONALLY LEFT BLANK.